

Optogenetic activation of septal cholinergic neurons suppresses sharp wave ripples and enhances theta oscillations in the hippocampus

Marie Vandecasteele^{a,b}, Viktor Varga^{a,c}, Antal Berényi^{a,d,e}, Edit Papp^c, Péter Barthó^c, Laurent Venance^b, Tamás F. Freund^c, and György Buzsáki^{a,d,1}

^aCenter for Molecular and Behavioral Neuroscience, Rutgers University, Newark, NJ 07102; ^bCenter for Interdisciplinary Research in Biology, Institut National de la Santé et de la Recherche Médicale U1050, Centre National de la Recherche Scientifique, Unité Mixte de Recherche 7241, Collège de France, F-75005 Paris, France; ^cInstitute of Experimental Medicine, Hungarian Academy of Sciences, H-1083, Budapest, Hungary; ^dNeuroscience Institute, School of Medicine, New York University, New York, NY 10016; and ^eMTA-SZTE "Momentum" Oscillatory Neuronal Networks Research Group, Department of Physiology, University of Szeged, H-6720, Szeged, Hungary

Edited by Ranulfo Romo, Universidad Nacional Autónoma de México, Mexico City, D.F., Mexico, and approved August 5, 2014 (received for review June 25, 2014)

Theta oscillations in the limbic system depend on the integrity of the medial septum. The different populations of medial septal neurons (cholinergic and GABAergic) are assumed to affect different aspects of theta oscillations. Using optogenetic stimulation of cholinergic neurons in ChAT-Cre mice, we investigated their effects on hippocampal local field potentials in both anesthetized and behaving mice. Cholinergic stimulation completely blocked sharp wave ripples and strongly suppressed the power of both slow oscillations (0.5–2 Hz in anesthetized, 0.5–4 Hz in behaving animals) and supratheta (6–10 Hz in anesthetized, 10–25 Hz in behaving animals) bands. The same stimulation robustly increased both the power and coherence of theta oscillations (2–6 Hz) in urethane-anesthetized mice. In behaving mice, cholinergic stimulation was less effective in the theta (4–10 Hz) band yet it also increased the ratio of theta/slow oscillation and theta coherence. The effects on gamma oscillations largely mirrored those of theta. These findings show that medial septal cholinergic activation can both enhance theta rhythm and suppress peri-theta frequency bands, allowing theta oscillations to dominate.

acetylcholine | channelrhodopsin-2 | silicon probe | in vivo electrophysiology

Subcortical neuromodulators play a critical role in shifting states of the brain (1, 2). State changes can occur both during sleep and in the waking animal and are instrumental in affecting local circuit computation that supports various functions, including attention, learning, memory, and action (3–5). The septo-hippocampal cholinergic system has been hypothesized to play a critical role in setting network states in the limbic system (4, 6). ACh can affect both short- and long-term plasticity of synaptic connections and provide favorable conditions for encoding information (7–9). These plastic states are associated with hippocampal theta oscillations (10). High theta states are characterized by increased release of ACh that varies in a task-dependent manner on the time scale of seconds (11–13). In contrast, reduced cholinergic activity allows effective spread of excitation in the recurrent CA3 network, giving rise to synchronous sharp wave ripples (SPW-R) (14–16).

Inactivation of the medial septum (MS)/diagonal band of Broca abolishes theta oscillations in the hippocampus and entorhinal cortex (17) and results in severe learning deficit (18, 19). Similarly, selective toxin lesion of septal cholinergic neurons produces a several-fold decrease of theta power but not its frequency (20). The phase of the local field potentials (LFP) theta oscillations shifts from the septal to the temporal pole and in the CA3-CA1 axis by ~180° (21, 22). Thus, at each point in time neurons residing at different locations of the three-dimensional structure of the hippocampus spike at different theta phases yet are bound together by the global theta signal. These numerous sources of theta generators are believed to be coordinated by the reciprocal connections between the septum and hippocampus (23), but the nature of this spatial-temporal coordination is not well

understood (24). Both cholinergic and GABAergic neurons, and a small fraction of VGlut2 immunoreactive neurons (25), are believed to play a critical role in such global coordination (26, 27). Although GABAergic neurons of the MS were demonstrated to be entrained at theta frequency, identified cholinergic neurons did not show theta-related discharge pattern (28, 29). Additionally, both GABAergic and cholinergic neurons are affected by the feedback long-range hippocampo-septal inhibitory connections (30).

Early studies, performed in anesthetized animals, already suggested a critical role for the cholinergic septo-hippocampal projection in the generation of theta oscillations (6). Indeed, the low-frequency theta present under urethane anesthesia can be fully abolished by antimuscarinic drugs (31). In contrast, atropine or scopolamine fail to abolish theta oscillations during waking exploration (31, 32), although they affect the theta waveform and its amplitude-phase depth profile in the hippocampus (33). Although these previous works are compatible with the hypothesis that the role of septal cholinergic projections is mainly permissive and affects theta power without modulating its frequency (20, 26, 28), direct evidence is missing. The role of septal cholinergic neurons on gamma oscillation and SPW-R is even less understood (14). To address these issues, we used optogenetic activation of septal cholinergic input and examined its impact on hippocampal theta, peri-theta bands, gamma, and ripple oscillations in both anesthetized and freely moving mice.

Significance

Theta oscillations are a prominent rhythm of the brain occurring during active behavior and rapid eye movement sleep and thought to provide the temporal frame for the encoding of information. Acetylcholine modulation is a major player in hippocampal theta rhythm, as demonstrated by lesion and pharmacological manipulations of cholinergic receptors, yet the link between the activity of septal cholinergic neurons and the theta rhythm is not fully understood. We used specific optogenetic stimulation of the septo-hippocampal cholinergic neurons in the anesthetized and behaving mouse to decipher the effects of cholinergic stimulation on hippocampal network activity and show that in addition to promoting theta oscillations it suppresses sharp wave ripples and peri-theta band activity.

Author contributions: M.V., V.V., and G.B. designed research; M.V., V.V., A.B., and E.P. performed research; L.V. and T.F.F. contributed new reagents/analytic tools; P.B., L.V., and T.F.F. provided a physiology setup; M.V., V.V., E.P., and P.B. analyzed data; and M.V., V.V., and G.B. wrote the paper.

The authors declare no conflict of interest.

This article is a PNAS Direct Submission.

¹To whom correspondence should be addressed. Email: Gyorgy.Buzsaki@nyu.edu.

This article contains supporting information online at www.pnas.org/lookup/suppl/doi:10.1073/pnas.1411233111/-DCSupplemental.

Results

To address the role of the septo-hippocampal cholinergic input, we used mice expressing light-activated cation channel channelrhodopsin-2 tagged with a fluorescent protein (ChR2-YFP) under the control of the choline-acetyl transferase promoter (ChAT). These mice displayed an intense YFP-positive staining in MS ChAT neurons, as shown by double immunostaining in transgenic hybrid (Fig. 1A) and virus-injected mice (Fig. S1A) and YFP- and ChAT-positive fibers in the target structures of the MS, including the hippocampus (Fig. S1B).

Light-Responsive Cells in the Medial Septum. First, using urethane-anesthetized mice, we verified that illumination of the MS induced a light-entrained activity of putative ChAT neurons. To this end, we constructed optrodes by placing an etched and sharpened optic fiber (diameter $<10\text{ }\mu\text{m}$) glued on the shank(s) of a multisite silicon probe (34). Brief pulses of light (10–100 ms) were applied at 0.5 Hz continuously while the optrode was descended into the MS (Fig. S1C), until responsive units were identified. Responsive neurons reliably followed trains of pulses (Fig. 1C1) and sine stimulations between 0.5 and 12 Hz (Fig. 1D), whereas at frequencies >10 Hz spike adaptation was observed (Fig. 1C2). All light-responsive cells ($n = 6$ cells from $n = 4$ mice) had slow spontaneous firing rates (median firing rate 0.57 Hz, range 0.04–1.9 Hz). Half of the driven cells significantly increased their firing frequency in response to a tail pinch although they stayed within a slow-firing range (<4 Hz; Fig. 1B), consistent with the typical activity of cholinergic neurons (28, 29).

Hippocampal Responses to MS Stimulation. Whereas cholinergic neurons faithfully followed the frequency of stimulation, the frequency of theta oscillation in the hippocampus was not affected (Fig. 1E). To ensure that this effect was not due to the low intensity of light delivered by the optrode (<0.6 mW at the tip), in subsequent experiments a multimode optic fiber (50- to 105- μm core, yielding 5–10 mW maximal light intensity) was implanted in the MS and multisite, linear silicon probes were used to record hippocampal activity in anesthetized and freely moving mice.

Suppression of hippocampal sharp wave ripples. The most prominent and consistent effect of optogenetic stimulation of MS cholinergic neurons was the suppression of SPW-Rs recorded in the CA1 pyramidal layer (Fig. 2). Ripple occurrence was significantly suppressed or abolished during MS stimulation (1–12 Hz, sine stimulation or pulse trains, 1–60 s) in mice recorded either during urethane anesthesia ($n = 6$ mice, median suppression –90%, $P = 0.0312$) or during free behavior ($n = 8$, median suppression –92%, $P < 0.01$). The few surviving SPW-Rs during the stimulation were similar to ripples detected in control epochs (Fig. S2). The effective suppression of SPW-Rs demonstrated that MS stimulation exerted a physiological impact on the operations of hippocampal circuits in both anesthetized and behaving mice.

Effect on hippocampal LFP power. MS stimulation had an apparently differential effect on theta oscillations in anesthetized and behaving mice. Whereas under both conditions MS stimulation reduced the power in the slow (0.5–2 Hz in anesthetized, 0.5–4 Hz in behaving animals) and supratheta bands (6–10 Hz in anesthetized, 10–25 Hz in behaving animals), it increased theta power in anesthetized mice but it decreased or had no effect on theta power in behaving mice (Fig. 3).

Under anesthesia, stimulation of the MS typically switched hippocampal activity from large-amplitude, irregular activity (35) to a theta state (Fig. 3A). Spectral analysis of 10-s-long stimulation segments relative to 10-s control segments before stimulation (Fig. 3B and C) showed that the MS stimulation effect was most prominent at lower frequencies (<30 Hz). Optogenetic stimulation induced a strong increase of power at 3–4 Hz (“urethane theta,” ref. 31), whereas both lower (0.5–2 Hz) and upper (6–10 Hz) neighboring frequency bands were strongly decreased. The impact on theta was most prominent in stratum lacunosum-moleculare (LM, Fig. 3C). Across animals, the effect on theta power increase was significant individually in six of seven anesthetized mice (2–6 Hz;

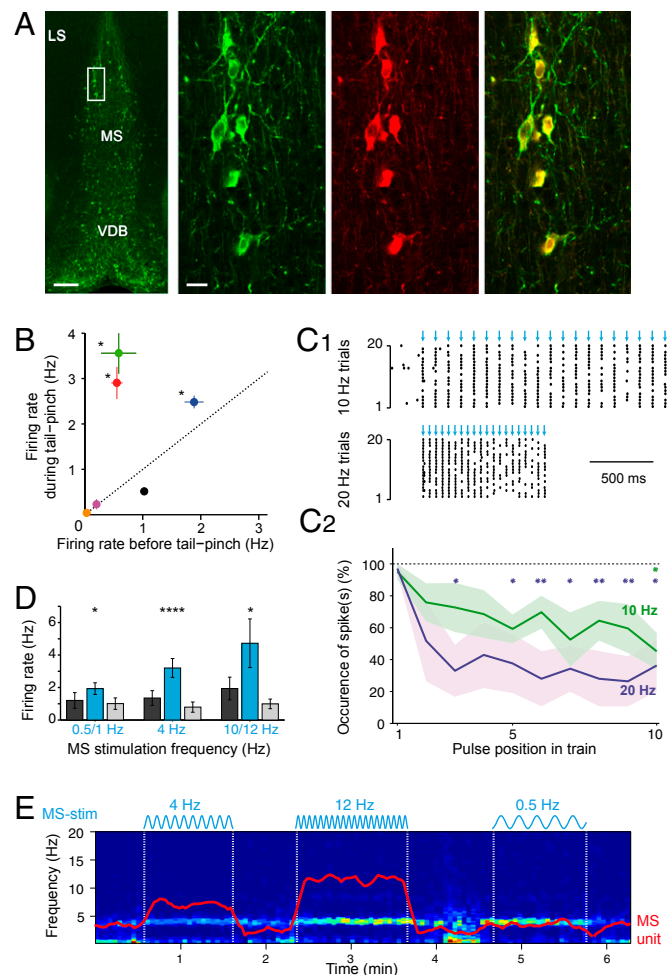


Fig. 1. Entrainment of MS neurons by blue light stimulation. (A) Left-most panel: YFP-positive immunostaining in a coronal section of the MS in a ChAT-ChR2-YFP hybrid transgenic mouse. LS, lateral septum; VDB, ventral diagonal band. (Scale bar: 200 μm .) Right panels: higher magnification of the MS (rectangle in left panel), double immunostaining of YFP (green, left), and ChAT (red, middle), showing their perfect colocalization (overlay, right; 100% overlap in $n = 108$ and $n = 111$ neurons in two mice). (Scale bar: 10 μm .) (B) Spontaneous activity of all light-entrained cells. Asterisks indicate a significant difference in the mean firing rate in response to tail pinch (mean \pm SEM, $n = 4$ trials, paired t test). (C1) Raster plot activity of an entrained cell in response to 10 Hz (Upper) and 20 Hz (Lower) trains of optogenetic stimulations (15-ms pulses, blue arrows). (C2) The reliability of spiking decreases at higher frequencies (mean \pm SEM, $n = 4$ neurons). Asterisks indicate a significantly lower spike occurrence compared with the first pulse (repeated-measures ANOVA with Bonferroni post-hoc test). (D) Mean firing rates of MS entrained cells in response to sinusoidal stimulations. Asterisks indicate significant differences between control and stimulation epochs ($n = 5$ cells tested during spontaneous and tail pinch-evoked activity, repeated-measures ANOVA with Bonferroni post-hoc test). (E) Spectrogram of hippocampal LFP in LM during sine stimulation of the MS. Red: mean firing rate of a simultaneously recorded MS unit (same y axis scale as the spectrogram). * $P < 0.05$, ** $P < 0.01$, *** $P < 0.001$, **** $P < 10^{-4}$.

group median change +1.5 dB, $P < 10^{-21}$, $n = 296$ trials; Fig. S3A). Stimulation also significantly decreased power in the slow oscillation band (0.5–2 Hz; -3.5 dB, $P < 10^{-31}$) and in the supratheta band (6–10 Hz; -0.9 dB, $P < 10^{-11}$). Optogenetic stimulation in the MS of ChAT-cre mice injected by a virus carrying only the fluorescent reporter enhanced YFP (EYFP) induced no detectable changes in hippocampal activity (Fig. S4).

The theta/slow oscillation ratio increased in six out of seven anesthetized mice (group: +207%, $P < 10^{-33}$). To further analyze

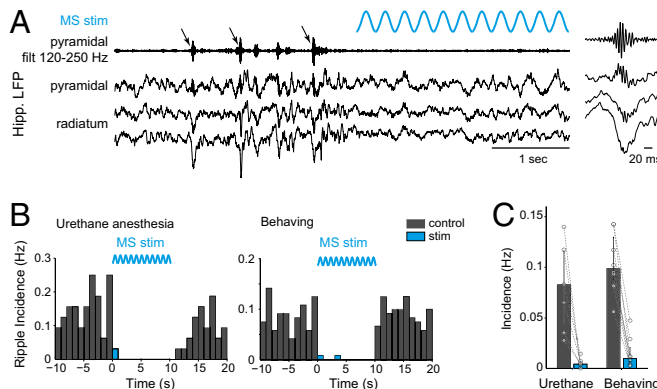


Fig. 2. MS stimulation suppresses hippocampal sharp wave ripples. (*A*) Example of hippocampal LFP in the pyramidal layer and stratum radiatum displaying SPW-R (arrows) before the onset of optogenetic stimulation. (*Inset*) Magnification of a detected ripple. (*B*) Peristimulus time histogram of ripple occurrence, before, during, and after 10-s sine stimulations at 1–12 Hz, recorded in the same mouse under urethane anesthesia (*Left*, $n = 77$ trials) or during free behavior (*Right*, $n = 128$ trials). (*C*) The mean incidence of ripples is significantly decreased during stimulation in both urethane anesthesia ($n = 6$ mice) and freely moving conditions ($n = 8$ mice). Bars/error bars, medians and quartiles for all animals; paired dots, individual mice.

this effect at a finer timescale, we used wavelet decomposition to identify theta epochs within each control and stimulation epoch: Each sample was classified as theta-dominated if the scale corresponding to the maximal coefficient of the wavelet decomposition fell into theta band (2–6 Hz for anesthesia). We found that the proportion of theta-dominated samples per epoch was significantly increased by optogenetic stimulation of MS cholinergic neurons in all mice (median proportion increase $+0.33$, $P < 10^{-32}$, $n = 296$ trials; $n = 7$ mice, range: $+0.08$ to $+0.64$; see also Fig. S5).

In waking, freely moving mice, MS stimulation significantly decreased the power in the slow oscillation (0.5–4 Hz; -1.5 dB, $P < 10^{-18}$) and supratheta (10–25 Hz; -1.6 dB, $P < 10^{-38}$) bands (Fig. 3*B* and *C*). In contrast to that in anesthetized mice, theta power (4–10 Hz) in waking, freely moving mice was moderately but significantly decreased (median change -0.8 dB, $P < 10^{-28}$, $n = 417$ trials, $n = 4$ mice, range -0.2 to -1.4 dB). However, the theta/slow oscillation ratio increased significantly (median: $+15\%$, $P = 0.0024$). In addition, the median proportion of theta-dominated samples per epoch increased from 0.30 in control to 0.43 in stimulation epochs ($P < 10^{-7}$; see also Fig. S5). Therefore, even though theta power was decreased, the stronger effect on peri-theta bands concurred to increase relative theta prominence in the LFP.

In two mice, recordings were performed in both anesthetized and behaving conditions (example in Fig. 3*B*). Changes in these mice reflected the group effects presented above and further demonstrated the differential effect of cholinergic stimulation on theta oscillation between anesthetized and drug-free animals.

Cholinergic activation effects on gamma-band oscillations were largely similar to those on theta-band oscillations, albeit with lower magnitude. Under anesthesia, the slow gamma oscillations (<40 Hz) increased in multiple layers, whereas gamma power (both slow, 30–70 Hz and midgamma, 70–100 Hz) decreased in waking animals (Fig. S6*A–C*). Theta phase modulation of gamma power was not altered by optogenetic stimulation (Fig. S6*D*).

Effect on hippocampal LFP coherence. The theta-promoting effect of MS stimulation was further confirmed by coherence analysis across hippocampal layers (Fig. 4). In particular, stratum radiatum (Rad)-LM coherence increased at 3–4 Hz during stimulation under anesthesia and in the 2- to 7-Hz band in behaving animals [Fig. 4*A* and Fig. S3*B*; median change in theta band: $+0.09$ in anesthetized animals (2–6 Hz), $P < 10^{-25}$, individually significant in six of seven animals; $+0.06$ in behaving animals (4–10 Hz), individually significant in four of four mice]. The MS

stimulation-induced coherence increase in theta band under anesthesia (2–6 Hz) was significant across all layer pairs, whereas in the behaving animal (4–10 Hz) it was confined to Rad-LM and oriens-pyramidal layer pairs (Fig. 4*B*). The induced coherence increase in behaving animals was restricted to frequencies below 7 Hz, indicating that cholinergic activation of the hippocampus selectively affected the slow form of theta oscillations (31). The induced power and coherence changes of the LFP described above were largely confirmed by analyzing spectral changes of current source density signals as well (Fig. S7).

To examine the impact of the frequency of MS stimulation, we compared trials with 1-, 4-, 8-, and 12-Hz trains. In no experiment did we observe that the frequency of the hippocampal LFP followed the frequency of MS stimulation (Fig. 1*E* and Fig. S8). In several cases, increasing the frequency of stimulation increased the magnitude of power changes (Fig. S8). This effect is likely due to the fact that faster stimulation induced more spikes and therefore higher levels of ACh released from the cholinergic terminals in the hippocampus (36).

State dependence of MS stimulation effect. Visual inspection of the LFP traces indicated that the relative magnitude of the MS stimulation-induced effects depended on background hippocampal activity. Because the strongest effect was the suppression

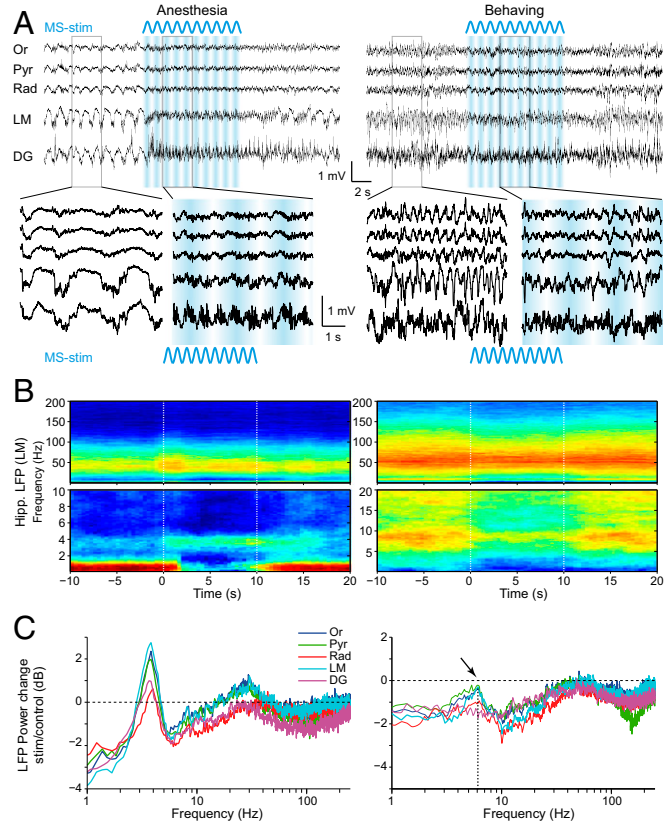


Fig. 3. MS stimulation exerts a selective effect at theta and peri-theta frequencies in both anesthetized (*Left*) and behaving (*Right*) mouse. (*A*) Example of hippocampal LFP from five layers. Blue: MS sinusoidal stimulation. (*Lower*) magnified view of 3 s from control and stimulation epochs. (*B*) Spectrograms of LFP recorded in LM in the same mouse under both conditions before, during, and after 10-s sine stimulation (median of $n = 71$ trials in anesthesia, $n = 82$ in behaving). LFP was whitened for better visualization of higher frequencies. (*Lower*) Zoom on lower frequencies. (*C*) LFP power change in hippocampal layers (median of all trials, $n = 296$ in seven anesthetized mice, $n = 417$ in four behaving mice). Arrow and dotted line indicates the spared (least suppressed) frequency (~6 Hz). DG, dentate gyrus; LM, stratum lacunosum-moleculare; Or, stratum oriens; Pyr, pyramidal layer; Rad, stratum radiatum.

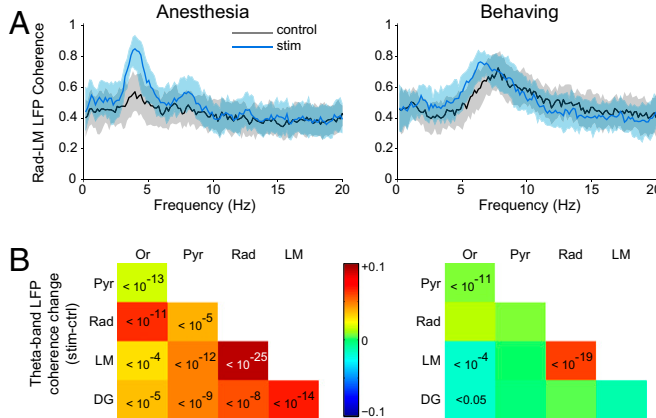


Fig. 4. MS stimulation promotes hippocampal theta coherence. (*A*) Rad-LM coherence spectrum in control (black) and stimulation (blue) epochs in representative animals (median \pm quartiles of all trials, $n = 98$ in anesthesia, $n = 82$ in behaving). (*B*) MS stimulation-induced coherence change for theta band (anesthesia: 2–6 Hz, behaving: 4–10 Hz). For each layer pair, the color indicates the median change (all trials pooled), and significant P values are indicated (Wilcoxon's rank sum test with Bonferroni's correction for 10 layer pairs).

of SPW-Rs, we segregated trials into two groups: those displaying at least one ripple event during the control period (10 s preceding the onset of stimulation, “ripple trials”) and those without ripples and with a dominant power in the theta band (“theta-dominant trials”). Because theta and SPW-Rs do not rapidly alternate (37), the presence of SPW-Rs in the prestimulation epochs can be taken as an indication of a different overall state compared with epochs with prominent theta oscillations. In anesthetized animals, LFP power in LM showed a larger relative effect of stimulation in ripple trials than in theta-dominant trials (Fig. 5*A* and *B*; theta/slow oscillation ratio in ripple trials: +402%, $P < 10^{-11}$, $n = 69$ trials vs. theta-dominant trials: +155%, $P < 10^{-6}$, $n = 84$ trials). The differential effect of stimulation was also apparent in the changes of dominant frequency. In ripple trials, the median frequency shifted from a slow-oscillation range to theta band (from 1.1 to 3.8 Hz, $P < 10^{-10}$), whereas stimulation did not affect the median frequency in theta-dominant trials (3.7 Hz in both control and stimulation epochs; $P > 0.1$; Fig. 5*B*).

MS stimulation also exerted a background state-dependent differential effect in behaving mice. In ripple trials, MS stimulation induced a global decrease in LFP power with a relative sparing at ~ 6 Hz, resulting in a moderate but significant increase in the theta/slow oscillation ratio (Fig. 5*C* and *D*; +27%; $P < 10^{-11}$, $n = 165$ trials) and also increased theta proportion during the stimulation epoch (Fig. 5*D*). The dominant frequency increased significantly from 3.8 Hz to 6 Hz during stimulation ($P = 0.0012$; Fig. 5*D*). In contrast, during theta-dominant trials the theta/slow oscillation ratio and the proportion of theta samples were not significantly changed, and theta frequency was significantly decreased (from 7.3 Hz to 6.9 Hz, $P < 10^{-3}$). The power in the supratheta (10–25 Hz) band was significantly reduced in both ripple (-47% , $P < 10^{-23}$) and theta-dominant (-21% , $P < 10^{-11}$) trials.

It may be argued that SPW-Rs events are more likely followed by theta epochs and, conversely, epochs with high theta power may be more likely followed by epochs with low theta power. To control for such potential sampling bias, we compared pairs of consecutive 10-s epochs of spontaneous activity in the same way as control vs. stimulation epoch pairs were analyzed. Epochs were pseudorandomly chosen by shifting the analyzed epochs by -20 s (i.e., comparing a “pre” interval located -30 to -20 s before stimulation onset to a “post” interval located -20 to -10 s before the stimulation onset). The lack of significant changes in these control analyses confirmed the validity of our statistical analyses of the MS-induced effects (Fig. S9). In summary, optogenetic activation of MS cholinergic neurons was more

effective in the absence of background theta activity. When background epochs were already dominated by high theta power, MS stimulation induced only moderate or no effects.

Behavioral Effects of MS Stimulation. To assess the behavioral correlates of the physiological effects observed on hippocampal activity, we measured locomotor activity on a linear track or in an open field in three behaving mice equipped with movement-tracking light-emitting diodes during stimulation (Fig. 6). Considering the dichotomy of the MS stimulation effect depending on background LFP activity (discussed in *State dependence of MS stimulation effect*), we similarly segregated LFP epochs into ripple trials vs. theta-dominant trials. During ripple trials, associated with lower locomotor activity, MS stimulation significantly increased speed in two of the three mice. In contrast, in theta-dominant trials, speed was decreased significantly during stimulation compared with control epochs in two of the three mice. Therefore, the dichotomous effects on behavior were consistent with the effects on theta power described above. The correlations between locomotion speed and theta power and speed and theta frequency were preserved during MS stimulation (Fig. 6*C*). These findings indicate that optogenetic cholinergic activation did not alter the relationship between theta and behavior.

Discussion

Optogenetic stimulation of the cholinergic septal neurons induced theta and gamma oscillations in the urethane-anesthetized mouse. However, in waking, exploring mice the impact of stimulation on theta and gamma oscillations was less expressed and largely masked by the faster, noncholinergic form of theta. The strongest effects of cholinergic stimulation were observed on abolishing SPW-Rs and reducing the power of slow and supratheta oscillations under both anesthesia and waking state. Thus, a main effect of ACh in theta oscillations seems to be the reduction of competing nontheta mechanisms.

The most consistent effect of optogenetic activation of septal cholinergic neurons was the suppression of SPW-Rs (Fig. 2). Because such an effect was observed in every session in both anesthetized and waking animals, SPW-R suppression most clearly illustrates the effectiveness of optogenetic stimulation. These findings support the hypothesis that SPW-Rs are initiated by the excitatory recurrent collaterals of CA3 pyramidal neurons when subcortical controlling neuromodulatory transmitters are reduced (14). ACh may attenuate the spread of such excitation by reducing

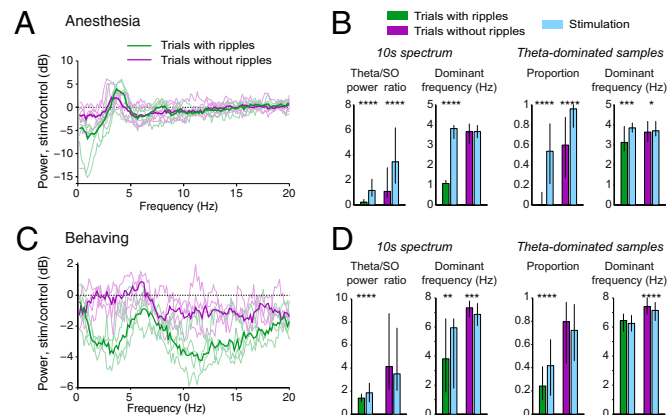


Fig. 5. Brain state dependence of MS stimulation effect. Recordings from anesthetized (*A* and *B*) and behaving (*C* and *D*) mice. (*A* and *C*) LFP power change in LM in ripple (green) versus theta (purple) trials. Thick lines: median of all trials; thin lines: individual animals. (*B* and *D*) Stimulation effect in each type of trials for (left to right) theta/slow oscillation ratio, spectral dominant frequency, proportion of theta-dominated samples, and median frequency of theta-dominated samples. * $P < 0.05$, ** $P < 0.01$, *** $P < 0.001$, **** $P < 10^{-4}$.

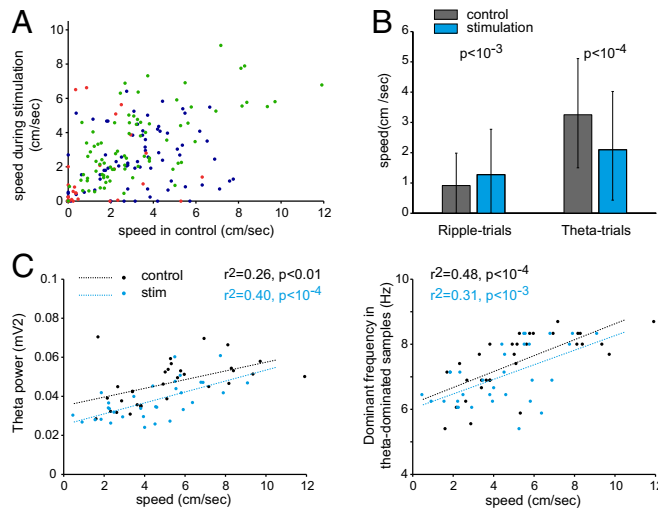


Fig. 6. Effect of MS stimulation on locomotor behavior. (A) Mean locomotion speed during control and stimulation epochs. Each dot is a single trial; colors: data for three individual mice. (B) Effect on mean locomotor speed during ripple trials ($n = 90$, three mice pooled) and theta-dominant trials ($n = 129$). (C) Correlation between speed and theta power (Left) or theta-dominant frequency (Right) in mouse 2, in control (black dots and line fit) and stimulation epochs (blue dots and line fit). Pearson's correlation coefficient and P values are indicated.

the release of glutamate from the presynaptic terminals of CA3 neurons (38, 39). In support of this hypothesis, adding the muscarinic drug carbachol to the perfusion solution in *in vitro* investigation also abolishes spontaneously occurring SPW-Rs (16). Alternatively, or in addition, suppression of hippocampal axo-axonic neurons by transiently bursting septal GABAergic neurons may initiate SPW-Rs (40). This suggestion, however, leaves open the question of why a specific subset of septal inhibitory cells bursts during reduced cholinergic activity in the absence of theta oscillation. Overall, these findings can explain the competing, antagonistic relationship between SPW-Rs and theta oscillations (14).

Our results provide direct support for the role of ACh in enhancing theta oscillations (20) and the distinction between cholinergic-muscarinic and noncholinergic mechanisms of theta oscillations (31). ChR2-expressing cholinergic septal neurons faithfully followed the frequency of optogenetic stimulation, although frequency attenuation was obvious above 10 Hz. However, the frequency of induced LFP theta oscillations was independent of the entrainment frequency of septal cholinergic cells (Fig. 1). The lack of frequency-driving ability of cholinergic neurons is not surprising in light of the slow, second messenger-mediated mechanism of muscarinic receptors (41). Increasing the frequency of optogenetic stimulation simply increased theta power; this effect can be explained by the higher discharge rates of the septal cholinergic cells. Frequency control of theta oscillations, instead, may depend on the rhythmic firing patterns of septo-hippocampal GABAergic neurons (26, 28), which terminate exclusively on hippocampal inhibitory interneurons (42).

Another robust effect of optogenetic activation of MS cholinergic neurons in both anesthetized and behaving mice was the suppression of the power of slow oscillations (Fig. 3). These findings are similar to stimulation of basal forebrain cholinergic neurons, which reduced LFP power in the primary visual cortex in the 1- to 5-Hz band (43). One might argue that the reduction of hippocampal power in this band simply reflected changes in volume-conducted slow-frequency signals from the neocortex. However, previous work has demonstrated that slow oscillations also affect hippocampal circuits, as reflected by the entrained firing patterns (44, 45). Furthermore, MS cholinergic neurons do not project outside the limbic system (46), and thus their activation is not

expected to exert a direct impact on neocortical activity. In addition to SPW-Rs and slow oscillations, optogenetic stimulation of the MS also suppressed power in the supratheta frequency band. These observations parallel the competing effects between theta and supratheta band activity because termination of theta-associated exploration in the intact animal is regularly coupled with enhanced “beta” power (47). The mechanisms of the suppressive effects of ACh on these oscillations are likely similar in the hippocampus and neocortex (43) and may be mediated, at least partially, by pre-synaptic M2 cholinergic receptor-mediated blockade of GABA release from basket and other interneurons (48).

Optogenetically induced activation of cholinergic neurons consistently increased low-frequency theta power and across-layer theta coherence in the anesthetized mouse, independent of whether stimulation occurred in the absence or presence of ongoing spontaneous theta activity (Figs. 3 and 4), as expected under the framework of the cholinergic model of theta generation (31, 49). A related interpretation of the differential effects of optogenetic stimulation of MS during anesthesia and waking is that the overall tone of ACh is lower under urethane than in the waking animal (50, 51). Thus, optogenetically assisted increase of cholinergic activity could increase ACh release effectively in the anesthetized mouse, as illustrated by the robust power changes in various frequency bands, but the same stimulation would exert fewer effects in the waking animal when levels of ACh are already high. The largest induced effect was observed in LM, a layer with a high density of cholinergic terminals (52) that were confirmed to be expressing ChR-2 in our immunostaining experiments. The same stimulation exerted a less clear effect on theta oscillations in the drug-free, behaving animal, because theta seen during movement is largely noncholinergically mediated, whereas the cholinergic input provides a background of sensory input-related drive to the hippocampus during movement. The effect of MS optogenetic drive was still observed by a significant increase of theta coherence between stratum Rad and LM below 7 Hz. These observations agree well with noncholinergic and cholinergic distinctions of theta oscillations related to motor and sensory integration, respectively (53). Overall, our findings provide perhaps the best example to date for a competition between cholinergic and noncholinergic types of theta rhythms during movement. They also demonstrate that the observed relationship between optogenetic stimulation of septal cholinergic cells and LFP power changes was not mediated by changes of motor behavior, because optogenetic stimulation of MS did not exert a consistent effect on locomotion speed, supporting previous observations (54).

Overall, cholinergic activation suppressed SPW-Rs entirely, strongly reduced the power of slow oscillations and supratheta frequency oscillations, and increased theta power and coherence when the background activity contained little theta power. The relative enhancement of theta activity was thus largely due to the suppression of frequencies surrounding the theta band. In contrast, optogenetic activation brought about very little change in any frequency band when the background was characterized by high theta power. These results suggest that in the exploring and ambulating animal ACh release already maximally activates muscarinic receptors and, therefore, additional activation of septal cholinergic neurons has little impact.

Methods

Details on experimental procedures are provided in *Supporting Information*. Briefly, we used ChAT-Cre transgenic mice ($n = 23$) expressing ChR2 in their cholinergic neurons. The cre-dependent ChR2-containing construct was delivered to the MS either by viral gene transfer or by crossing the ChAT-Cre line with a ChR2-carrying floxed reporter line. ChAT-Cre mice injected with a control viral vector containing only the fluorescent reporter YFP were used as control for the effect of light ($n = 3$). Optical stimulation was achieved by transmitting light from a 473-nm laser source via an optic fiber to the MS. Both square pulse and sine wave stimulation were applied at frequencies from 0.5 to 20 Hz (pulse) or 0.5–12 Hz (sine). Multisite silicone probes were used for recording hippocampal local field potentials from several layers of the CA1-dentate axis in the dorsal hippocampus. LFP signal from all layers was spectrally decomposed and effect of stimulation on various frequency bands was determined before and after MS stimulation in both anesthetized and freely moving mice.

ACKNOWLEDGMENTS. We thank Győző Goda, Emőke Simon, Daniel English, Clémence Delarbre, Anne-Marie Godeheu, and Audrey Hay for assistance; Michaël Zugaro for comments on the manuscript; and Nikon Microscopy Center at the Institute of Experimental Medicine, Nikon Austria GmbH, and Auro-Science Consulting Ltd. for technical support. This work was supported by National Institutes of Health Grants NS-34994, MH-54671, and NS074015; National Science Foundation Grant 0542013; the J. D. McDonnell Foundation; European Union's

Marie Curie Actions Grant FP7-PIOF-GA-2008-221834; European Union Framework Program 7 - European Research Council (EU-FP7-ERC)-2013 Starting Grant 337075; EU-FP7-ERC-2011 Advanced Grant 294313; Fondation pour la Recherche Médicale Grant SPE20061209127; Lendület program of the Hungarian Academy of Sciences and Human Frontiers Science Program Grant STF-000244/2009; Hungarian Scientific Research Fund Grant OTKA NF101773; and the National Brain Program of Hungary.

- Harris KD, Thiele A (2011) Cortical state and attention. *Nat Rev Neurosci* 12(9):509–523.
- Lee SH, Dan Y (2012) Neuromodulation of brain states. *Neuron* 76(1):209–222.
- Jones BE (2005) From waking to sleeping: Neuronal and chemical substrates. *Trends Pharmacol Sci* 26(11):578–586.
- Hasselmo ME, McGaughy J (2004) High acetylcholine levels set circuit dynamics for attention and encoding and low acetylcholine levels set dynamics for consolidation. *Prog Brain Res* 145:207–231.
- Rasch B, Born J (2013) About sleep's role in memory. *Physiol Rev* 93(2):681–766.
- Stumpf C, Petsche H, Gogolak G (1962) The significance of the rabbit's septum as a relay station between the midbrain and the hippocampus. II. The differential influence of drugs upon both the septal cell firing pattern and the hippocampus theta activity. *Electroencephalogr Clin Neurophysiol* 14:212–219.
- Patil MM, Linster C, Lubenov E, Hasselmo ME (1998) Cholinergic agonist carbachol enables associative long-term potentiation in piriform cortex slices. *J Neurophysiol* 80(5):2467–2474.
- Ovsepian SV, Anwyl R, Rowan MJ (2004) Endogenous acetylcholine lowers the threshold for long-term potentiation induction in the CA1 area through muscarinic receptor activation: *in vivo* study. *Eur J Neurosci* 20(5):1267–1275.
- Leung LS, Shen B, Rajakumar N, Ma J (2003) Cholinergic activity enhances hippocampal long-term potentiation in CA1 during walking in rats. *J Neurosci* 23(28):9297–9304.
- Buzsáki G (2002) Theta oscillations in the hippocampus. *Neuron* 33(3):325–340.
- Parikh V, Kozak R, Martinez V, Sarter M (2007) Prefrontal acetylcholine release controls cue detection on multiple timescales. *Neuron* 56(1):141–154.
- Marrosu F, et al. (1995) Microdialysis measurement of cortical and hippocampal acetylcholine release during sleep-wake cycle in freely moving cats. *Brain Res* 671(2):329–332.
- Zhang H, Lin SC, Nicolelis MA (2010) Spatiotemporal coupling between hippocampal acetylcholine release and theta oscillations *in vivo*. *J Neurosci* 30(40):13431–13440.
- Buzsáki G, Leung LW, Vanderwolf CH (1983) Cellular bases of hippocampal EEG in the behaving rat. *Brain Res* 287(2):139–171.
- Norimoto H, Mizunuma M, Ishikawa D, Matsuki N, Ikegaya Y (2012) Muscarinic receptor activation disrupts hippocampal sharp wave-ripples. *Brain Res* 1461:1–9.
- Zylla MM, Zhang X, Reichinnek S, Draguhn A, Both M (2013) Cholinergic plasticity of oscillating neuronal assemblies in mouse hippocampal slices. *PLoS ONE* 8(11):e80718.
- Lawson VH, Bland BH (1993) The role of the septohippocampal pathway in the regulation of hippocampal field activity and behavior: Analysis by the intraseptal microinfusion of carbachol, atropine, and procaine. *Exp Neurol* 120(1):132–144.
- Leutgeb S, Mizumori SJ (1999) Excitotoxic septal lesions result in spatial memory deficits and altered flexibility of hippocampal single-unit representations. *J Neurosci* 19(15):6661–6672.
- Winson J (1978) Loss of hippocampal theta rhythm results in spatial memory deficit in the rat. *Science* 201(4351):160–163.
- Lee MG, Chrobak JJ, Sik A, Wiley RG, Buzsáki G (1994) Hippocampal theta activity following selective lesion of the septal cholinergic system. *Neuroscience* 62(4):1033–1047.
- Lubenov EV, Siapas AG (2009) Hippocampal theta oscillations are travelling waves. *Nature* 459(7246):534–539.
- Patel J, Fujisawa S, Berényi A, Royer S, Buzsáki G (2012) Traveling theta waves along the entire septotemporal axis of the hippocampus. *Neuron* 75(3):410–417.
- Wang XJ (2002) Pacemaker neurons for the theta rhythm and their synchronization in the septohippocampal reciprocal loop. *J Neurophysiol* 87(2):889–900.
- Geisler C, et al. (2010) Temporal delays among place cells determine the frequency of population theta oscillations in the hippocampus. *Proc Natl Acad Sci USA* 107(17):7957–7962.
- Huh CY, Goutagny R, Williams S (2010) Glutamatergic neurons of the mouse medial septum and diagonal band of Broca synaptically drive hippocampal pyramidal cells: Relevance for hippocampal theta rhythm. *J Neurosci* 30(47):15951–15961.
- Hangya B, Borhegyi Z, Szilágyi N, Freund TF, Varga V (2009) GABAergic neurons of the medial septum lead the hippocampal network during theta activity. *J Neurosci* 29(25):8094–8102.
- Dragoi G, Carpi D, Recce M, Csicsvari J, Buzsáki G (1999) Interactions between hippocampus and medial septum during sharp waves and theta oscillation in the behaving rat. *J Neurosci* 19(14):6191–6199.
- Simon AP, Poindessous-Jazat F, Dutar P, Epelbaum J, Bassant MH (2006) Firing properties of anatomically identified neurons in the medial septum of anesthetized and unanesthetized restrained rats. *J Neurosci* 26(35):9038–9046.
- Zhang H, Lin SC, Nicolelis MA (2011) A distinctive subpopulation of medial septal slow-firing neurons promote hippocampal activation and theta oscillations. *J Neurophysiol* 106(5):2749–2763.
- Tóth K, Borhegyi Z, Freund TF (1993) Postsynaptic targets of GABAergic hippocampal neurons in the medial septum-diagonal band of Broca complex. *J Neurosci* 13(9):3712–3724.
- Kramis R, Vanderwolf CH, Bland BH (1975) Two types of hippocampal rhythmic slow activity in both the rabbit and the rat: Relations to behavior and effects of atropine, diethyl ether, urethane, and pentobarbital. *Exp Neurol* 49(1 Pt 1):58–85.
- Newman EL, Gillet SN, Climer JR, Hasselmo ME (2013) Cholinergic blockade reduces theta-gamma phase amplitude coupling and speed modulation of theta frequency consistent with behavioral effects on encoding. *J Neurosci* 33(50):19635–19646.
- Buzsáki G, Czopf J, Kondákor I, Kellényi L (1986) Laminar distribution of hippocampal rhythmic slow activity (RSA) in the behaving rat: Current-source density analysis, effects of urethane and atropine. *Brain Res* 365(1):125–137.
- Royer S, et al. (2010) Multi-array silicon probes with integrated optical fibers: Light-assisted perturbation and recording of local neural circuits in the behaving animal. *Eur J Neurosci* 31(12):2279–2291.
- Soltesz I, Deschénes M (1993) Low- and high-frequency membrane potential oscillations during theta activity in CA1 and CA3 pyramidal neurons of the rat hippocampus under ketamine-xylazine anesthesia. *J Neurophysiol* 70(1):97–116.
- Colom LV, Ford RD, Bland BH (1987) Hippocampal formation neurons code the level of activation of the cholinergic septohippocampal pathway. *Brain Res* 410(1):12–20.
- Ylinen A, et al. (1995) Sharp wave-associated high-frequency oscillation (200 Hz) in the intact hippocampus: Network and intracellular mechanisms. *J Neurosci* 15(1 Pt 1):30–46.
- Fernández de Sevilla D, Cabezas C, de Prada AN, Sánchez-Jiménez A, Buño W (2002) Selective muscarinic regulation of functional glutamatergic Schaffer collateral synapses in rat CA1 pyramidal neurons. *J Physiol* 545(Pt 1):51–63.
- Hasselmo ME, Schnell E (1994) Laminar selectivity of the cholinergic suppression of synaptic transmission in rat hippocampal region CA1: Computational modeling and brain slice physiology. *J Neurosci* 14(6):3898–3914.
- Viney TJ, et al. (2013) Network state-dependent inhibition of identified hippocampal CA3 axo-axonic cells *in vivo*. *Nat Neurosci* 16(12):1802–1811.
- Eglen RM (2012) Overview of muscarinic receptor subtypes. *Handbook Exp Pharmacol* 208(208):3–28.
- Freund TF, Antal M (1988) GABA-containing neurons in the septum control inhibitory interneurons in the hippocampus. *Nature* 336(6195):170–173.
- Pinto L, et al. (2013) Fast modulation of visual perception by basal forebrain cholinergic neurons. *Nat Neurosci* 16(12):1857–1863.
- Wolansky T, Clement EA, Peters SR, Palczak MA, Dickson CT (2006) Hippocampal slow oscillation: A novel EEG state and its coordination with ongoing neocortical activity. *J Neurosci* 26(23):6213–6229.
- Isomura Y, et al. (2006) Integration and segregation of activity in entorhinal-hippocampal subregions by neocortical slow oscillations. *Neuron* 52(5):871–882.
- Gaykema RP, Luiten PG, Nyakas C, Traber J (1990) Cortical projection patterns of the medial septum-diagonal band complex. *J Comp Neurol* 293(1):103–124.
- Quinn JK, Nitz DA, Chiba AA (2010) Learning-dependent dynamics of beta-frequency oscillations in the basal forebrain of rats. *Eur J Neurosci* 32(9):1507–1515.
- Gulyás AI, et al. (2010) Parvalbumin-containing fast-spiking basket cells generate the field potential oscillations induced by cholinergic receptor activation in the hippocampus. *J Neurosci* 30(45):15134–15145.
- Lawrence JJ (2008) Cholinergic control of GABA release: Emerging parallels between neocortex and hippocampus. *Trends Neurosci* 31(7):317–327.
- Materi LM, Semba K (2001) Inhibition of synaptically evoked cortical acetylcholine release by intracortical glutamate: Involvement of GABAergic neurons. *Eur J Neurosci* 14(1):38–46.
- Clement EA, et al. (2008) Cyclic and sleep-like spontaneous alternations of brain state under urethane anesthesia. *PLoS ONE* 3:e2004.
- Frotscher M, Léránt C (1985) Cholinergic innervation of the rat hippocampus as revealed by choline acetyltransferase immunocytochemistry: A combined light and electron microscopic study. *J Comp Neurol* 239(2):237–246.
- Bland BH (2008) Anatomical, physiological, and pharmacological properties underlying hippocampal sensorimotor integration. *Information Processing by Neuronal Populations*, eds Hölscher C, Munk M (Cambridge Univ Press, Cambridge, UK), pp 283–325.
- Bland BH, Bird J, Jackson J, Natsume K (2006) Medial septal modulation of the ascending brainstem hippocampal synchronizing pathways in the freely moving rat. *Hippocampus* 16(1):11–19.

Supporting Information

Vandecasteele et al. 10.1073/pnas.1411233111

SI Methods

Animals. A total of 26 adult mice (2–7 mo) of both sexes were used in this study. Three transgenic mouse strains were used: 14 mice expressing the Cre-recombinase under the control of the choline acetyl-transferase promoter (ChAT-Cre, Jackson Labs strain 006410, or GENSAT GM60) were injected with Cre-dependent Channelrhodopsin2 (ChR2) or control viral vector (discussed below), whereas 9 mice were the offspring of the ChAT-Cre line crossed with the Ai32 reporter line carrying a Cre-dependent, enhanced YFP (EYFP)-tagged ChR2(H134R)-containing expression cassette (Allen Institute for Brain Research, or Jackson Labs, strain 12569). Three mice were offspring of ChAT-Cre mice crossed with Cre-reporter line Ai27, bearing a Cre-dependent ChR2(H134R)-tdTomato construct (Allen Institute) (see ref. 1 for details about Ai32 and Ai27 mouse strains). All experiments were performed in accordance with the National Institutes of Health *Guide for the Care and Use of Laboratory Animals*, the Institutional Ethical Codex, Hungarian Act of Animal Care and Experimentation (1998, XXVIII, section 243/1998), and the European Union guidelines (directive 2010/63/EU), and with the approval of the Institutional Animal Care and Use Committees at Rutgers University, New York University, the Institute for Experimental Medicine of the Hungarian Academy of Science, and the Center for Interdisciplinary Research in Biology. All mice were housed in 12:12 light/dark cycle. Water and food were available for ad libitum consumption. All efforts were made to minimize pain and suffering and to reduce the number of animals used.

Surgery. General anesthesia was induced with isoflurane inhalation. For acute recordings, anesthesia was maintained with urethane injection (1–1.5 mg/kg, i.p. initial injection, supplemented if necessary up to 2.2 mg/kg). For survival surgery (injection of virus, or implantation of probes and optic fibers), anesthesia was maintained with one i.p. injection of ketamine-xylazine (120 mg/kg and 16 mg/kg, respectively), followed by isoflurane inhalation delivered through a mask mounted on the stereotaxic apparatus. Body temperature was kept constant with a heating pad.

Virus injection. The surgeries were performed inside an isolation cabinet under biosafety level-2 (BSL-2) confinement or in a BSL-2 virus injection facility. Briefly, the skull was exposed under antiseptic conditions using local anesthesia with bupivacaine/lidocaine and a hole was drilled above the medial septum (MS) [anteroposterior (AP) +0.98 mm from bregma, mediolateral (ML) +0.9 mm, 14° angle insertion, or AP +0.8 mm, ML +0.7 mm, 10° angle insertion or AP +0.7–0.9 mm, midline insertion at 0° angle]. A glass pipette (30- to 50-μm tip) connected to a Nanoject II/Nanoliter 2000 microinjector (Drummond Scientific Co. or WPI Inc.), or alternatively, a cannula connected to a 10-μL Hamilton syringe was used to inject 0.05–0.7 μL of virus solution at one to five different depths between 3.8 and 4.6 mm (14° angle insertion) or between 2.8 and 4 mm (10° angle insertion), or at 3.0–3.4 mm (midline, 0° insertion), over 10–30 min. After injection the pipette was removed slowly (0.1 then 0.5-mm steps, 10-min waiting periods between each), the scalp was sutured, and injected mice were housed in BSL-2 quarantine for 2–4 wk before experimentation.

Acute and chronic implantations. The scalp was shaved after local anesthesia with bupivacaine/lidocaine and the skull was exposed in antiseptic conditions. Stereotaxic locations of the MS (AP +0.8 mm, ML +0.7 mm and 10° angle, or ML 0 mm and 0° angle insertion) and hippocampus (AP –1.7 to –2.5 mm from bregma, ML –1 to –2 mm) were marked on the skull. Two holes were

drilled over the cerebellum to insert the ground and reference miniature screws. Craniotomies were performed at marked locations, and dura was gently removed. After implantation of probes and optic fibers (discussed below), a paraffin-wax mixture was used to seal the craniotomies. For chronic implantations, extra steps were performed: One or two extra support screws were inserted in opposite skull plates and implants were secured to the skull using dental cement encompassing all screws, and protected by a grounded copper mesh. Appropriate suture and postoperative care of the wounds was ensured, and recordings began after 1 wk of recovery (see ref. 2 for detailed procedures of chronic surgery and recordings in rats).

Viral Constructs. Two adeno-associated viruses (AAV) were used, one bearing ChR-2 with a YFP reporter and a control virus bearing only the YFP reporter. Both viruses are based on the same double-floxed inverse ORF technology designed by Karl Deisseroth (Stanford University, Stanford, CA) and used with his permission (www.stanford.edu/group/dlab/optogenetics/sequence_info.html#dio): The ChR-2 virus EF1a.DIO.hChR2(H134R)-EYFP.WPRE.hGH construct was packaged into AAV serotypes 2, produced at Vector Biolabs and a gift from Tibor Koos (Center for Molecular and Behavioral Neuroscience, Rutgers University, Newark, NJ), or serotype 5, purchased from Penn Vector Core. The control virus, EF1a.DIO.EYFP.WPRE.hGH (27056; Addgene), was packaged into AAV serotype 1, bought from Penn Vector Core, a gift from Marco Diana (Institut de Biologie de l'Ecole Normale Supérieure, Paris), and diluted three times in sterile PBS before use.

Silicon Probes and Optic Fiber Implants. In the hippocampus, linear multichannel silicon probes (16 or 32 sites, 50- or 100-μm spacing; NeuroNexus) were inserted across the CA1–DG axis, at a 2.1- to 2.5-mm depth in 17 animals. In three animals, 16-site tetrode-like probes (2 × 2 or 4 × 1 tetrode; NeuroNexus) were mounted on a microdrive (see ref. 2 for microdrive details), inserted above CA1 pyramidal layer (1-mm depth) and progressively lowered during recovery down to the pyramidal layer (recognized by the presence of ripples and stronger unit activity). Silicon probes were painted with 2% DiI solution (Sigma) to facilitate the ex vivo localization confirmation. In the MS, for optogenetic stimulation only (16 animals), 125-μm-diameter optic fibers with a 50- to 105-μm core (Thorlabs) were implanted at a 3.0- to 3.5-mm depth (depending on the stereotaxic angle chosen). Before surgery, the optic fibers were stripped from the buffer layer and connectorized with 1.25-mm ceramic ferrules (extracted from LC connectors; Thorlabs). A pencil-shaped tip was obtained by etching 30' in hydrofluoric acid (Sigma) to facilitate the insertion in the brain. For recording entrained cells in the MS together with optogenetic stimulation (four animals), custom-made optrodes were used: 10- to 50-μm core optic fibers (Thorlabs) were stripped from buffer layer and progressively etched down to a 2- to 10-μm tip in hydrofluoric acid before being attached to 12- to 16-site tetrode-like silicon probes (NeuroNexus Tech) by UV light-curing epoxy (see refs. 3 and 4 for optrode construction details). Optrodes were lowered to 2.8 mm and then progressively until typical MS activity was encountered in response to tail pinch [local field potentials (LFP) theta rhythm, presence of theta-on or theta-burst unit activity].

Optogenetic Stimulation. Light from a 473-nm diode-pumped solid-state (DPSS) laser (Dreamasers) was collimated with a fiberport (Thorlabs) or delivered by a 475-nm laser diode light

source (FLS-475 nm–20 mW; DIPSI) into a custom patch cord (Thorlabs) connected to the brain-implanted optic fiber. Light intensity was driven by analog modulation of the DPSS power supply, using a Master-8 pulse stimulator (AMPI), a MATLAB-controlled DAQ-board (National Instruments or Measurement Computing Corp.), or a CED micro1401 mkII data acquisition system (Cambridge Electronic Devices) to generate square or sinusoidal pulses. For stimulation only of MS, maximum light intensity (crest of the sine wave, or plateau pulse amplitude) was adjusted using a photodiode power sensor coupled to a power meter (S130A and PM30 or S130C and PM100USB; Thorlabs), taking into account the patch cord-to-fiber coupling (measured before implantation of the fiber), to obtain a maximum of 5–10 mW at the tip of the fiber in the brain. For recording of entrained cells in MS using optrodes, owing to etching and diffraction of light by epoxy the maximum light at the tip of the fiber was <0.6 mW. Pulse trains consisted of 10- to 100-ms pulses delivered at various frequencies ranging between 0.5 and 20 Hz. During sine wave stimulation 0.5- to 12-Hz sinuses were delivered for 5–60 s.

Electrophysiological Recordings. Extracellular signal was amplified (20 \times) with a VLSI headstage (Plexon) and acquired continuously at 32.5 kHz using a multichannel DigiLynx system (Neuralynx) or amplified, multiplexed, and acquired continuously at 20 kHz using a multichannel KJE-1001 system (5) (Amplipex) and stored for offline analysis (discussed below). Twelve animals underwent urethane acute recordings only (4 for MS-cells entrainment and 3 mice for control stimulation). Five animals underwent chronic recordings only. Two animals underwent recordings during the chronic implantation (during isoflurane anesthesia), followed by freely moving chronic recordings. One animal underwent chronic recordings followed by urethane acute recordings. For chronic recording, after postoperative recovery animals were recorded in their home cage during sleep, alert immobility, or actively awake (grooming, sniffing, etc.) and/or during the exploration of a different environment (1-m \times 7-cm linear track, baited with sucrose solution or water at each end, or a 60- \times 60-cm open field arena). Before linear track sessions mice were water-deprived for 1 d. Speed was monitored by video tracking coupled to the recording system.

Histological Processing. To confirm probe track location, animals were perfused transcardially under deep anesthesia with saline followed by fixative [4% (wt/vol) paraformaldehyde (PFA) or 10% (vol/vol) formaline solution]. Brain was removed and postfixed overnight in fixative then rinsed in PBS and cut to 60- to 80- μ m-thick coronal slices using a vibratome (VT1200; Leica). Slices were mounted in VectaShield (Vector Laboratories) to confirm probe track (aided by DiI) and optic fiber tracks.

For immunostaining, mice were deeply anesthetized with overdosed urethane and perfused transcardially by saline followed either by 4% PFA or by the Sloviter protocol [i.e., 2% (wt/vol) PFA in acetate buffer (pH 6.5) for 3 min followed by 2% (wt/vol) PFA in borate buffer (pH 8.5) for 40 min]. After perfusion brains were removed and stored in fixative solution overnight. Then, 50- μ m sections were prepared on a vibratome (Leica). Then, sections were washed in 0.1 M phosphate buffer (PB), cryoprotected overnight in 30% (wt/vol) sucrose dissolved in 0.1 M PB, and freeze-thawed in aluminum foil boats over liquid nitrogen to enhance penetration of the antisera. Next, after several changes of PB, the sections were transferred into Tris-buffered saline (TBS, pH 7.4). All of the following washes and antisera dilutions were carried out in TBS. Sections were incubated in primary antibody solution for two nights at 4 °C. Then, primary serum was washed, followed by incubation in secondary antibody solution for 3 h at room temperature, followed by extensive washing. Finally, sections were mounted on glass slides and covered by Vectashield.

Antibodies used were mouse monoclonal anti-ChAT primary (1:500; see ref. 6) and Alexa-647 conjugated donkey anti-mouse secondary (1:500) and chicken polyclonal anti-GFP primary (1:2,000; Life Technologies) and Alexa-488 conjugated goat anti-chicken secondary (1:500). In a subset of experiments, Rabbit polyclonal anti-parvalbumin (1:1,000; Swant) and Alexa 594-conjugated goat anti-rabbit secondary (1:500) were used. All secondaries were purchased from Life Technologies.

Sections were examined either by an A1R or C2 confocal laser scanning microscope (Nikon) or by an Axioplan-2 microscope (Zeiss). Photomicrographs were taken by the fluorescent detector of the A1R or C2 microscope, or by an Olympus DP-70 CCD camera (Olympus) on the Zeiss microscope. Adjustments of look-up tables of images were accomplished using Adobe Photoshop CS (Adobe Systems Inc.).

Data Analysis. Data were visualized and processed using NeuroScope and NDManger (7) (<http://neurosuite.sourceforge.net>) and analyzed by MATLAB (MathWorks) built-in or custom-built procedures. For unit detection in MS, single units were isolated from the wideband signal using the semiautomatic spike classifier KlustaKwik (<http://sourceforge.net/projects/klustakwik>) and further refined manually using the graphical spike sorting application Klusters (7) (<http://neurosuite.sourceforge.net>). Only units responding to light were analyzed. For analysis of the effect in hippocampus, mice with an optrode in the MS (four animals) are excluded from analysis, because the low light power emanating from the tip of the optrode would be unlikely to recruit a large and consistent enough population of cholinergic neurons to affect the hippocampus efficiently and reproducibly.

Multilayer Spectral Analysis. Only mice with linear probe recordings and a full optic fiber in the MS are included in multilayer analysis (10 anesthetized and 4 behaving mice). LFP signals were extracted from broadband signals by low-pass filtering at 1.25 kHz; malfunctioning channels were manually identified and excluded from analysis. The anatomical localization of each channel was then deduced from LFP features (ripples, sharp waves, and theta and gamma depth profile) as well as histological confirmation of the probe track, and five channels were chosen in each recording to represent the five layers analyzed: CA1 oriens, pyramidal, radiatum, stratum lacunosum-moleculare, and dentate gyrus (DG). DG sublayers were not distinguished because all were not similarly represented in all mice (in particular with 100- μ m-spacing linear probes). Current source density (CSD) was calculated as the second spatial derivative of the LFP (8) with a 100- μ m step. For CSD calculations, when needed, malfunctioning channels were replaced by the interpolation of the surrounding channels (in no case were there two contiguous bad channels). For each stimulation epoch, a control period of the same duration situated right before the stimulation period was defined. For each control and stimulation pair of epochs, the mean power and coherence spectrum of LFP and CSD signals were computed using multitaper Fourier analysis (9). When power ratios were used (theta/slow oscillation or low/medium gamma), the cumulative power over each band was normalized by the width of the band in hertz. The global dominant frequency of each epoch was taken as the frequency above 1 Hz with maximal power.

For theta-gamma phase-power coupling, LFP signal for each epoch was filtered at theta frequency (2–6 Hz for anesthesia, 4–10 Hz for drug-free) and at the chosen gamma subbands (20–40 or 40–80 Hz for anesthesia and 30–70 or 70–100 Hz for drug-free animals). Theta phase and gamma amplitude, respectively, were extracted using a Hilbert transform. The modulation index was computed using an adaptation of the Kullback–Leibler distance between the observed distribution and a uniform distribution, as described in ref. 10. The preferred phase was determined as the theta phase bin in which the maximal gamma power was observed.

For wavelet analysis, raw signal was down-sampled to 200 Hz to decrease computation load and then transformed by wavelet decomposition using a linear wavelet scale. Number of scales was 400 ranging from 0.5 to 100 Hz (minimum and maximum frequency in the decomposition). The continuous wavelet transform of the sampled time series x_n is a convolution of it with the wavelet function Ψ :

$$W_n(s) = \sum_{n'=0}^{N-1} x_{n'} \Psi^* \left[\frac{(n'-n)\delta t}{s} \right].$$

For the calculation of the wavelet power spectrum, the Morlet wavelet was used (11):

$$\Psi_0(\eta) = \pi^{-1/4} e^{i\omega_0\eta} e^{-\eta^2/2}.$$

For the wavelet decomposition the algorithm of Torrence and Compo was used (12). For each control and stimulation epoch we determined the theta-dominated LFP samples: time samples in which the dominant frequency (corresponding to the scale with maximal coefficient) was within theta band (2–6 Hz for anesthesia, 4–10 Hz for behaving). Theta proportion was calculated as the ratio of the number of theta-dominated samples over the total number of samples per epoch, and theta frequency as the median of the dominant frequencies of theta-dominated samples. Within each control and stimulation epoch theta segments were defined as segments composed of ≥ 100 (500 ms) contiguous theta-dominated samples. For state dependence, trials were segregated into two categories based on the presence of ripples and on the dominant frequency in the control epoch: “ripple trials” were characterized by the presence of at least one ripple in the control epoch, and “theta-dominant trials” by the absence of ripple in the control epoch together

with the control epoch dominant frequency (from Fourier analysis) within theta range (2–6 Hz for anesthesia, 4–10 Hz for behaving).

Ripple Analysis. For ripple detection, the 1.25-kHz down-sampled LFP signal in the pyramidal layer channel was band-pass-filtered (80–250 Hz) and ripple epochs were defined as periods during which ripple-band power was greater than mean ± 2 SD, with a peak power > 4 SD and a minimum duration of 40 ms. Thresholds were adjusted if needed after visual inspection of each recording. Sessions where no ripples were detected in the entire recording time were excluded from the ripple analysis (such as isoflurane anesthesia recordings). In the remaining sessions (from nine mice under urethane anesthesia, including three control mice, and eight behaving mice) all trials were included, independently of the presence or absence of ripples in each individual control epoch. The occurrence of ripples was then calculated for each mouse as the overall number of ripples in all control/stimulation periods divided by the overall duration of control/stimulation epochs.

Statistics. Unless otherwise stated, data are reported as medians and 25–75% quartiles, and statistical significance was computed using nonparametric paired tests when comparing control and stimulation epoch pairs (Wilcoxon’s signed rank test). Bonferroni’s correction for multiple testing was used when testing for five layers or 10 layer pairs. Statistics were computed using MATLAB or Prism (GraphPad Software). For circular data (preferred theta phase for theta-gamma coupling), the statistics were calculated using the Circular Statistics Toolbox for MATLAB (13). Data are presented as circular mean and distribution, and statistical testing of stimulation effect (control vs. stimulation epoch pairs) is computed by testing the median of the stimulation-control circular distance against 0 with a binomial test.

1. Madisen L, et al. (2012) A toolbox of Cre-dependent optogenetic transgenic mice for light-induced activation and silencing. *Nat Neurosci* 15(5):793–802.
2. Vandecasteele M, et al. (2012) Large-scale recording of neurons by movable silicon probes in behaving rodents. *J Vis Exp* 61(61):e3568.
3. Stark E, Koos T, Buzsáki G (2012) Diode probes for spatiotemporal optical control of multiple neurons in freely moving animals. *J Neurophysiol* 108(1):349–363.
4. Royer S, et al. (2010) Multi-array silicon probes with integrated optical fibers: Light-assisted perturbation and recording of local neural circuits in the behaving animal. *Eur J Neurosci* 31(12):2279–2291.
5. Berényi A, et al. (2014) Large-scale, high-density (up to 512 channels) recording of local circuits in behaving animals. *J Neurophysiol* 111(5):1132–1149.
6. Umbrico D, Watkins KC, Descarries L, Cozzari C, Hartman BK (1994) Ultrastructural and morphometric features of the acetylcholine innervation in adult rat parietal cortex: An electron microscopic study in serial sections. *J Comp Neurol* 348(3):351–373.
7. Hazan L, Zugaro M, Buzsáki G (2006) Klusters, NeuroScope, NDManager: A free software suite for neurophysiological data processing and visualization. *J Neurosci Methods* 155(2):207–216.
8. Mitzdorf U (1985) Current source-density method and application in cat cerebral cortex: Investigation of evoked potentials and EEG phenomena. *Physiol Rev* 65(1):37–100.
9. Mitra PP, Pesaran B (1999) Analysis of dynamic brain imaging data. *Biophys J* 76(2):691–708.
10. Tort ABL, et al. (2008) Dynamic cross-frequency couplings of local field potential oscillations in rat striatum and hippocampus during performance of a T-maze task. *Proc Natl Acad Sci USA* 105(51):20517–20522.
11. Muthuswamy J, Thakor NV (1998) Spectral analysis methods for neurological signals. *J Neurosci Methods* 83(1):1–14.
12. Torrence C, Compo GP (1998) A practical guide to wavelet analysis. *Bull Amer Meteor Soc* 79(1):61–78.
13. Berens P (2009) CircStat: A MATLAB toolbox for circular statistics. *J Stat Softw* 31:10.

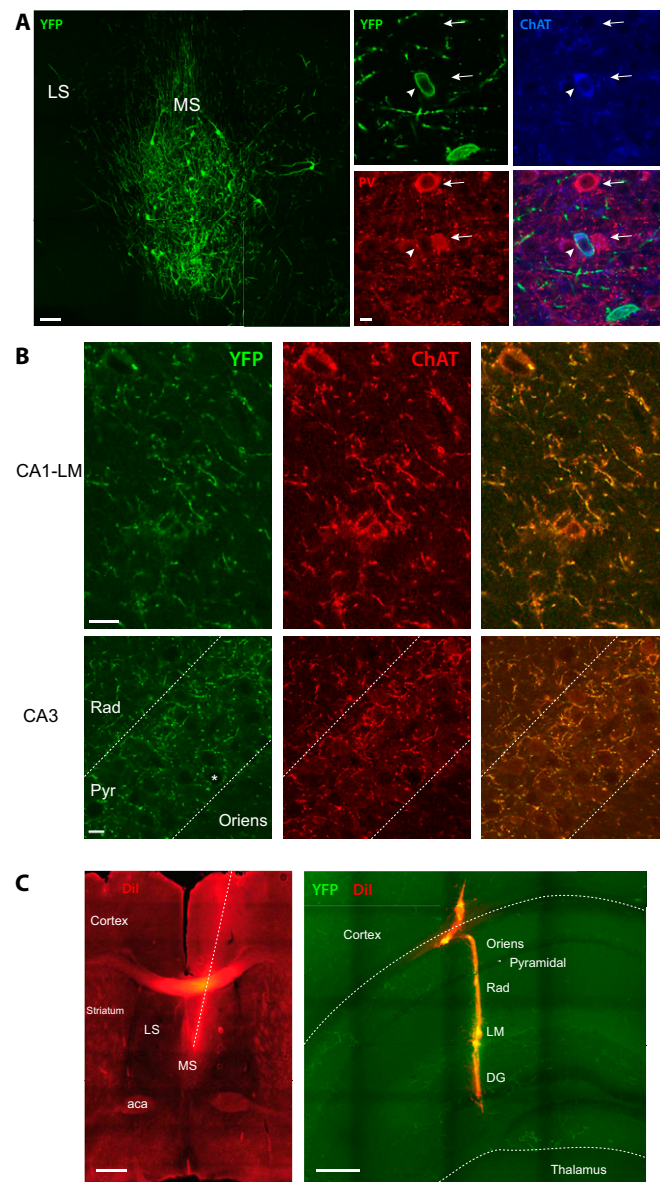


Fig. S1. (A) Left-most panel: YFP immunostaining in the MS of a ChAT-cre mouse injected with cre-dependent Chr2-YFP virus. (Scale bar: 100 μm .) Right panels: MS cells at higher magnification, showing the specific expression of YFP in ChAT neurons by triple immunostaining for YFP (green), ChAT (blue), and parvalbumin (red). Arrowhead: YFP-positive, ChAT-positive, and parvalbumin-negative cell body. Arrows: YFP-negative, ChAT-negative, and parvalbumin-positive cell bodies. (Scale bar: 10 μm .) (B) YFP- (green) and ChAT-positive (red) fibers in the CA1 stratum lacunosum-moleculare (*Upper*) and CA3 pyramidal layer (*Lower*). Asterisk indicates a putative pyramidal cell soma. (Scale bars: 10 μm .) (C) (*Left*) Optrode track (dotted line), revealed by Dil staining in a mouse with optogenetically entrained putative ChAT neurons in the MS. (Scale bar: 500 μm .) (*Right*) Dil-labeled track of hippocampal silicon probe spanning CA1 and DG regions. (Scale bar: 200 μm .) aca, anterior commissure; DG, dentate gyrus; LM, stratum lacunosum-moleculare; LS, lateral septum; MS, medial septum; PV, parvalbumin; Pyr, stratum pyramidale; Rad, stratum radiatum.

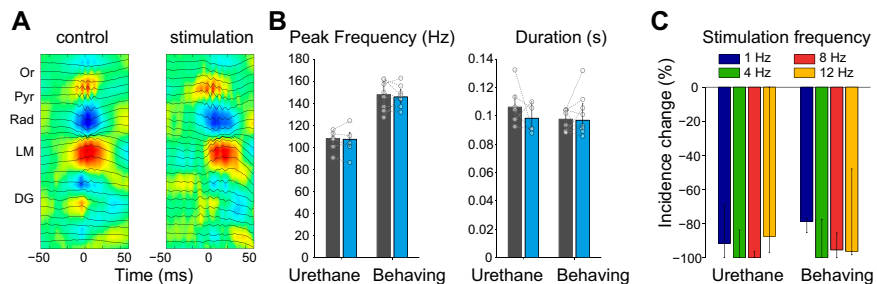


Fig. S2. (A) Sharp wave ripples detected in control (Left, triggered average of $n = 31$ ripple events) or during stimulation (Right, $n = 2$ ripple events) have similar LFP (black lines) and CSD (sources in red, sinks in blue). (B) The peak frequency (Left) and duration (Right) of ripples are unchanged during stimulation in all mice in both urethane anesthesia ($n = 6$ mice) and freely moving conditions ($n = 8$ mice). Bars/error bars are medians and quartiles for all animals, and paired dots represent individual mice. (C) Although the magnitude of suppression seemed less efficient for sinusoidal stimulations at 1 Hz than at higher frequencies (median and quartiles, all animals pooled), the frequency dependence was not significant (repeated-measures ANOVA, $P > 0.1$ in both conditions).

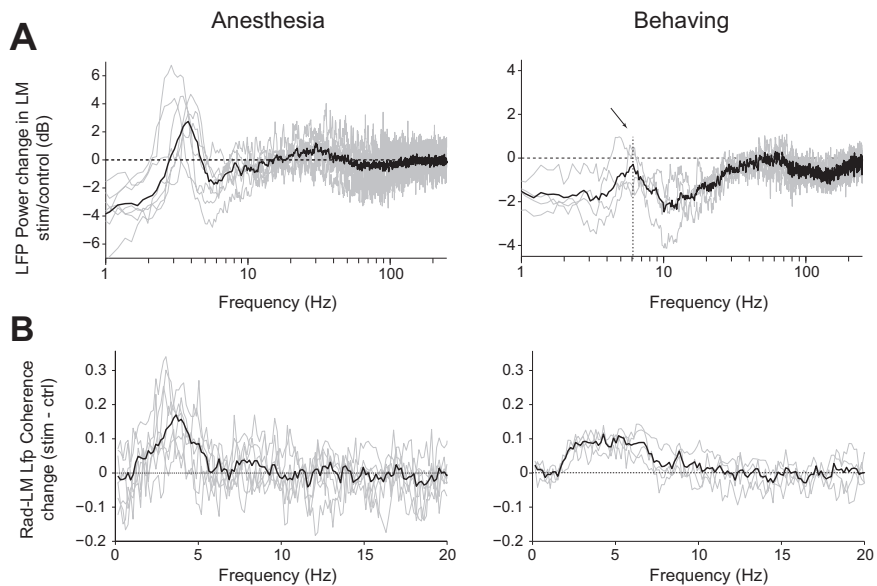
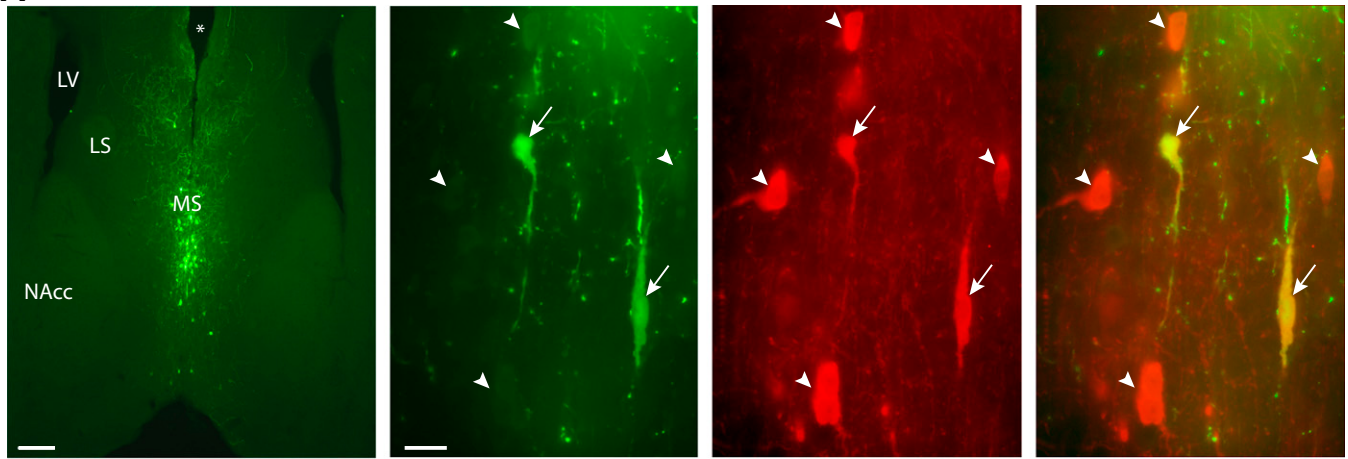
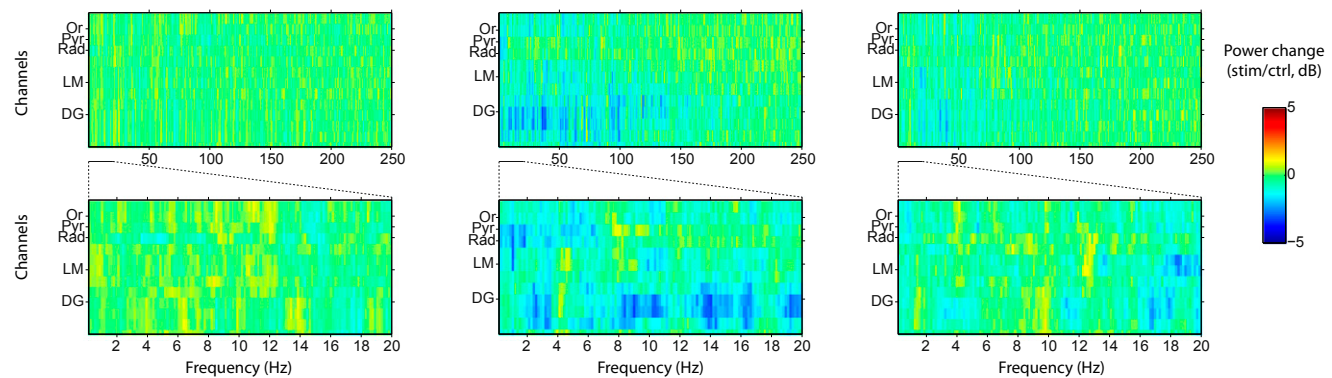


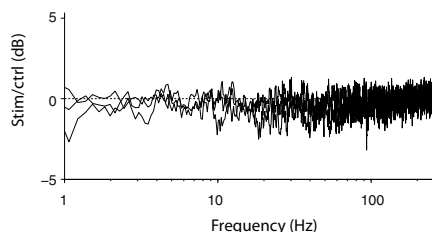
Fig. S3. Stimulation effects on LFP power in LM (A) and Rad-LM coherence (B) in each individual animal (thin gray lines) with the median across animals (thick black line).

A**B**

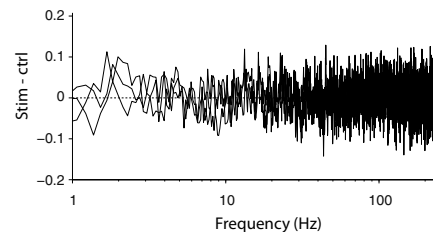
Lfp Power Change, ChAT-YFP, n=3 mice

**C**

Power change in LM



Coherence change, Rad-LM



Ripple occurrence (Hz)

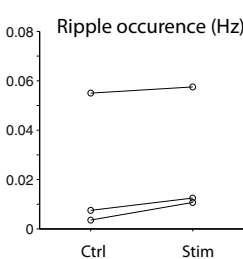


Fig. S4. Optogenetic stimulation of MS in urethane-anesthetized ChAT-YFP animals does not affect hippocampal activity. (A) Specific expression of YFP in ChAT neurons, as revealed by double immunostaining for ChAT (red) and YFP (green). Left-most panel: ChAT-cre mouse injected with YFP-only virus, showing YFP expression in the MS at low magnification. Asterisk indicates injection cannula and optic fiber track. (Scale bar: 200 μ m.) Right panels: MS of the same mouse at higher magnification, showing the specific expression of the YFP in ChAT-positive neurons (arrows). Arrowheads are YFP-negative ChAT neurons. LS, lateral septum; LV, lateral ventricle; MS, medial septum; NAcc, nucleus accumbens. (Scale bar: 20 μ m.) (B) Optogenetic stimulation of the MS (10-s-long sine wave at 1, 4, 8, or 12 Hz, median of 40 trials, maximum power output 9.4 mW) triggers no visible effect on the hippocampal LFP in urethane-anesthetized mice expressing YFP-only in ChAT neurons ($n = 3$ animals, each column is a different mouse). Recording sites are linearly arranged with 100- μ m spacing. (C) Optogenetic stimulation in urethane-anesthetized ChAT-YFP mice fails to trigger three main effects observed in ChAT-ChR2-YFP animals: No change is observable in LFP power in stratum lacunosum-molecular (LM, Left) or in Rad-LM coherence (Center). Optogenetic stimulation had no effect on ripple occurrence either (Right).

control
stim

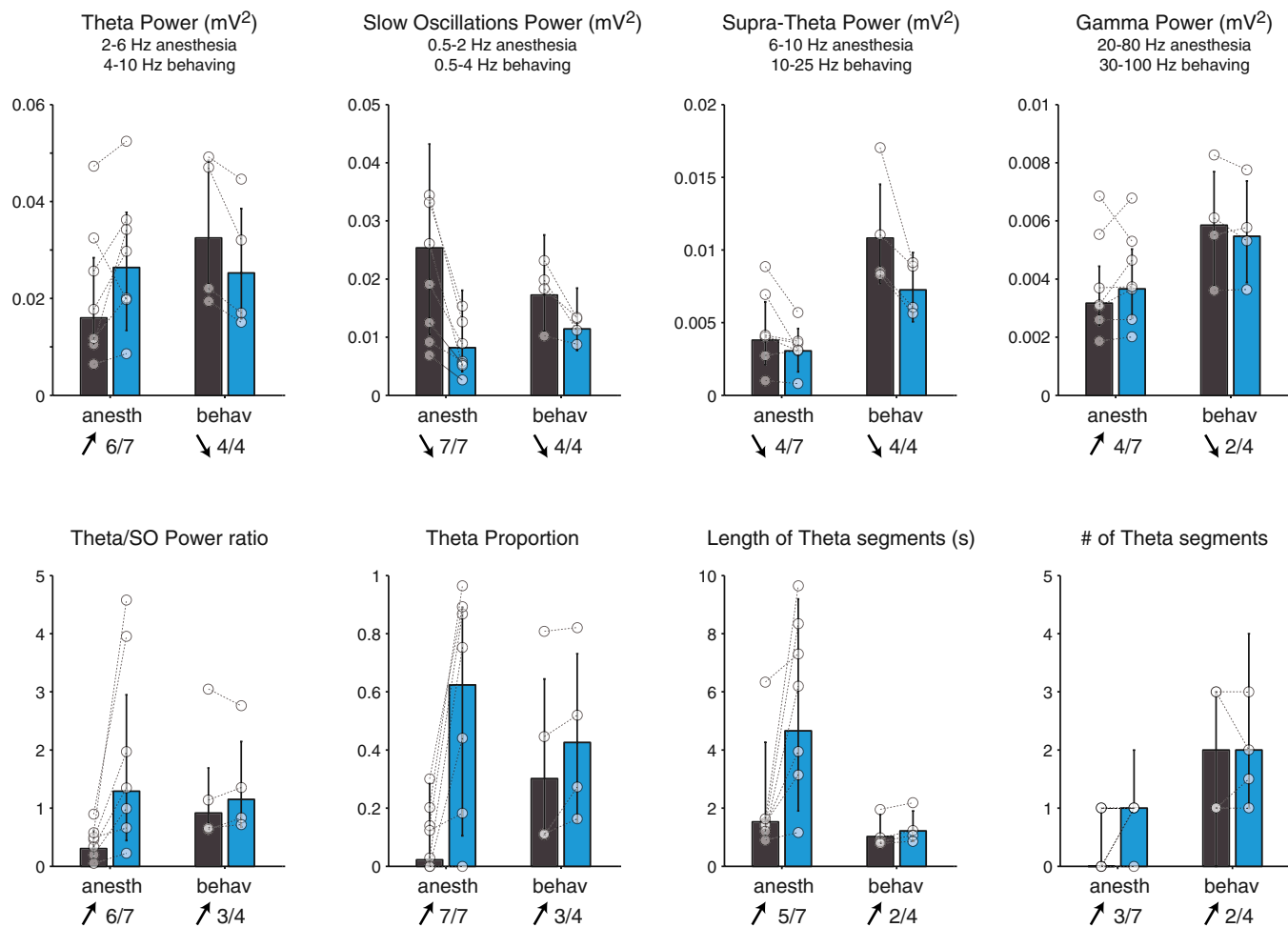


Fig. S5. Quantification of hippocampal LFP power changes induced by MS stimulation (10-s sinusoidal stimulation, 1–12 Hz). Bars represent the median and quartiles of all mice (all trials pooled); paired dots represent each animal; numbers below each condition indicate the proportion of animals displaying an individually significant change in the indicated direction.

ANESTHETIZED

BEHAVING

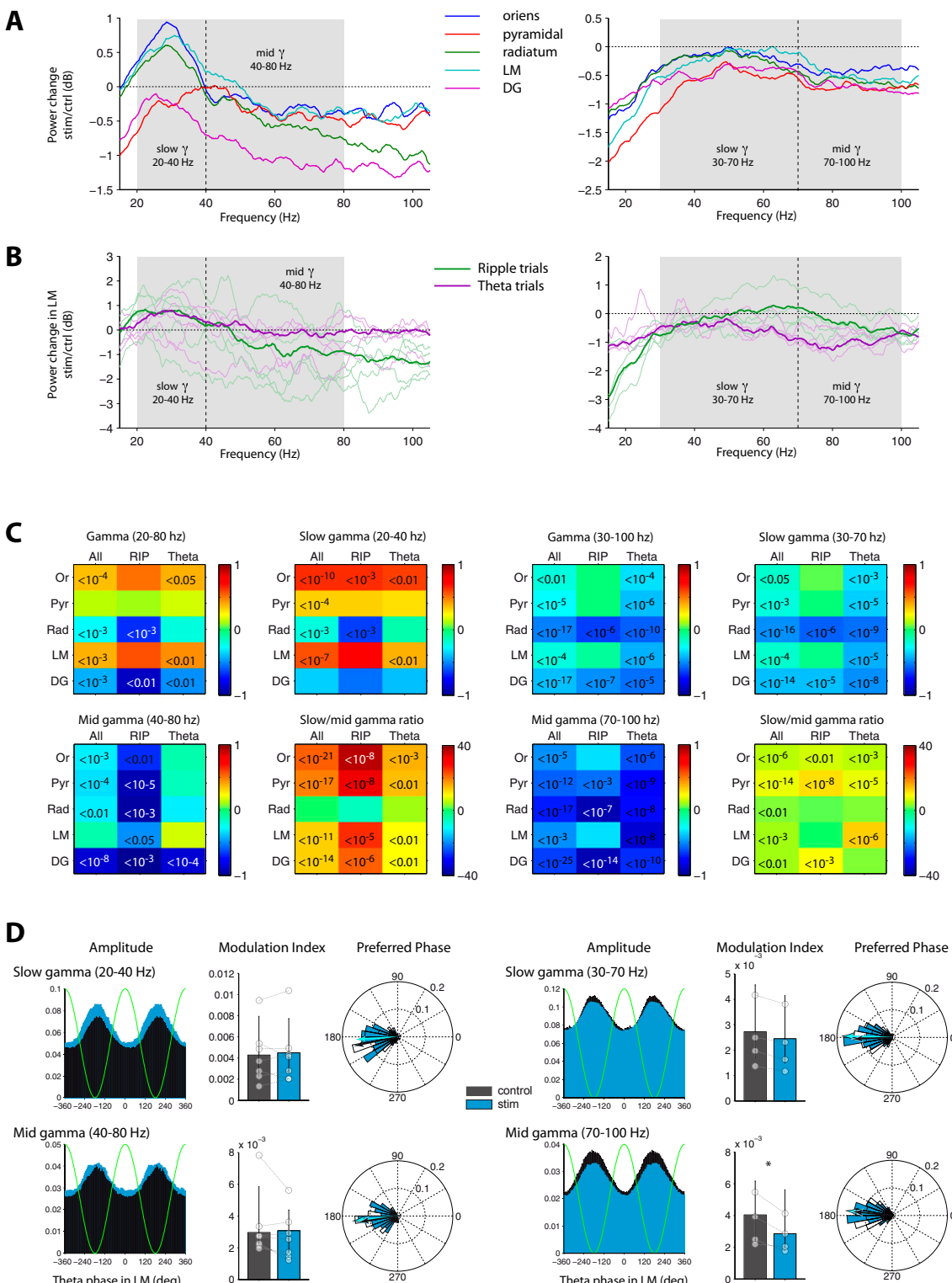
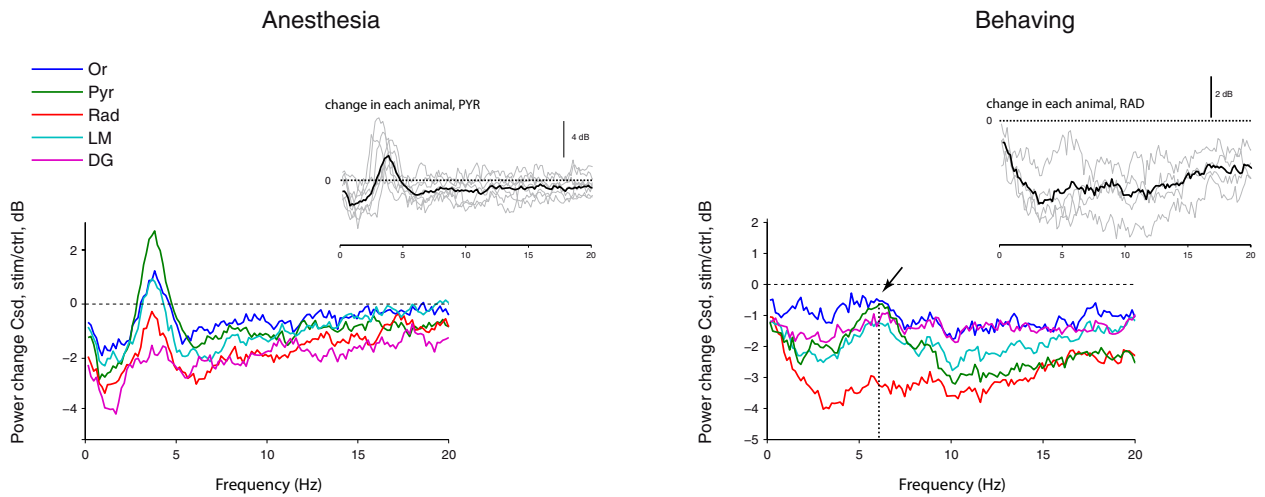
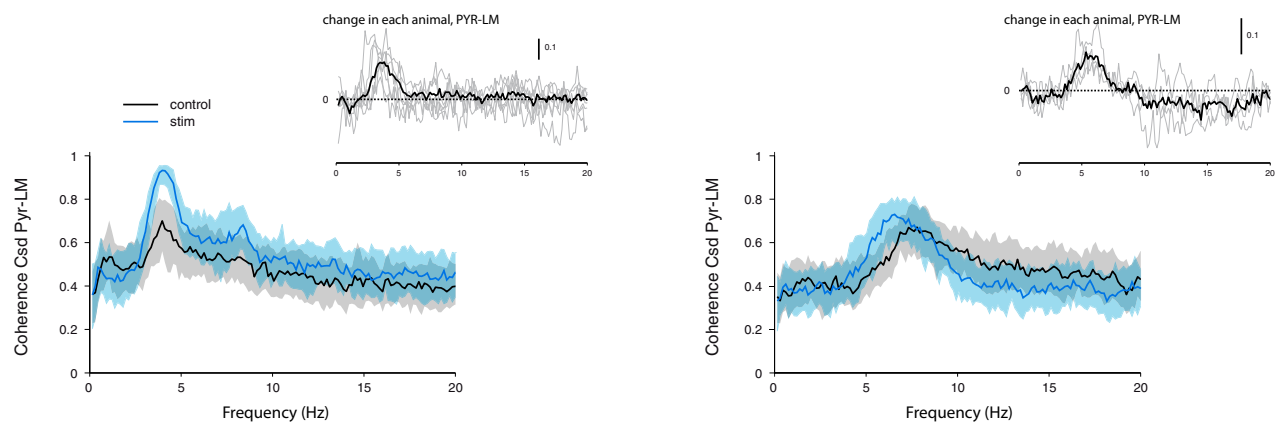
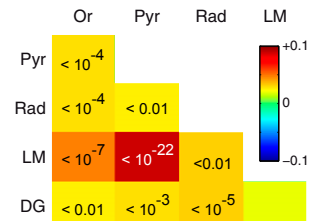


Fig. S6. Effect of MS stimulation on hippocampal gamma power and theta-gamma coupling in anesthetized (left column) and behaving (right column) mice. (A) LFP power changes in the gamma band in different layers (median power change, all trials pooled, $n = 296$ trials from seven anesthetized mice, $n = 417$ trials from four behaving animals). (B) LFP gamma power change in stratum lacunosum-moleculare (LM), segregated according to the brain state during the control epoch. The thick line represents the median across all trials ($n = 69$ and $n = 84$ for ripple and theta trials, respectively, under anesthesia, $n = 165$ and $n = 159$ in drug-free); thin lines correspond to individual animals. (C) Comparison of gamma change induced by optogenetic stimulation of the MS in five hippocampal layers, in all trials, ripple trials (RIP), and theta trials. For each condition, the three top-left, top-right, and bottom-left color plots represent gamma power change in the entire gamma band, slow gamma band, and mid-gamma band, respectively (median change across trials, decibels). The bottom right color legend continued on following page

plot represents the change (in percent of control) in the ratio of slow/mid-gamma power. In each color plot the color indicates the median change; number indicates the *P* value for the significant changes (Wilcoxon's rank sum test with Bonferroni correction for five layers). (*D*) Comparison of theta–gamma coupling in LM during control (black) and stimulation (blue) epochs for each gamma subband (slow gamma: *Upper*; mid-gamma: *Lower*) in anesthetized (left column) and behaving (right column) animals. The amplitude of gamma was plotted against theta phase (*Left*). From this distribution, the modulation index (*Center*) and the preferred phase (*Right*) were computed and compared in control and stimulation epochs. **P* < 0.05 (Wilcoxon's rank sum test with Bonferroni correction for five layers). The decrease in LM modulation index was not significant when individual animals were considered. Note that the differential changes in the gamma-band of anesthetized and waking mice are reminiscent of the changes observed in theta band (see Fig. 3).

A**B****C**

median change (stim-ctrl)



median change (stim-ctrl)

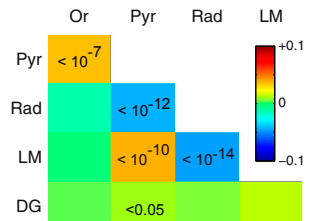


Fig. S7. Effect of MS stimulation on hippocampal CSD power and coherence in anesthetized (left column) and behaving (right column) mice. (A) CSD power changes in different layers (all trials pooled). Arrow and vertical line indicate the spared theta frequency in Pyr layer for behaving animals. (Insets) Change in the most affected layer (thick line, group; thin lines, individual animals): Pyr in anesthesia: median CSD power change in theta band +1.4 dB ($P < 10^{-24}$, $n = 296$ trials, individually significant in six out of seven mice), and Rad in behaving mice: median CSD power change in theta band -2.7 dB ($P < 10^{-45}$, $n = 417$ trials, individually significant in four of four mice). Note that the effect on Rad CSD in behaving animals is two- to fivefold stronger than in other layers, whereas the effect in LFP power was in the same range across layers (see Fig. 3C). (B) CSD coherence between Pyr and LM in control (black) and stimulation (blue) epochs, median of all trials in representative animals ($n = 98$ in an anesthetized animal, $n = 82$ in a behaving animal; interquartile area is shaded). (Insets) Pyr-LM coherence change in all animals (thick lines), and each individual animal (thin lines). (C) CSD coherence change in theta band for each hippocampal layer pair. In each square, the color indicates the median change (all trials pooled); the number indicates the P value for the significant changes (Wilcoxon's rank sum test, with Bonferroni's correction for 10 layer pairs).

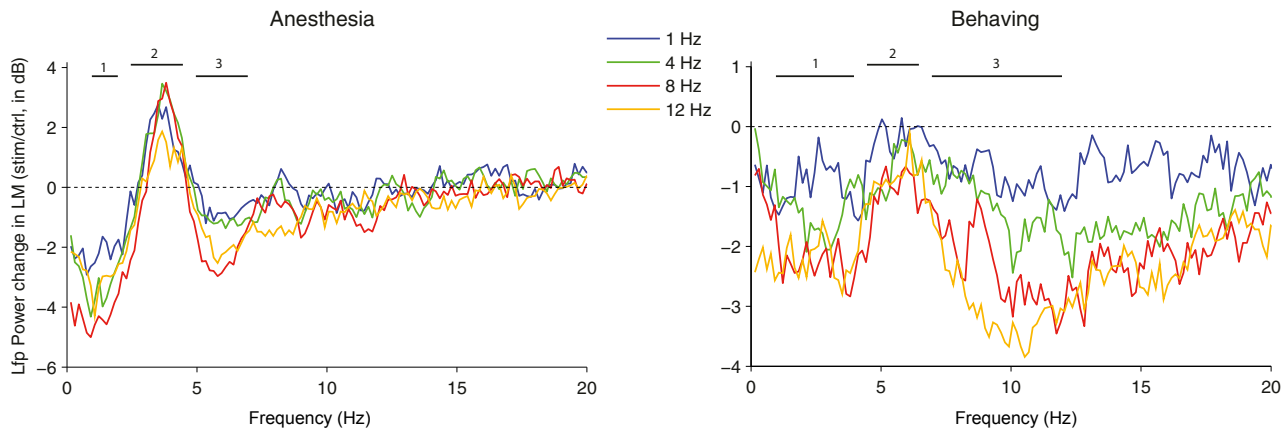
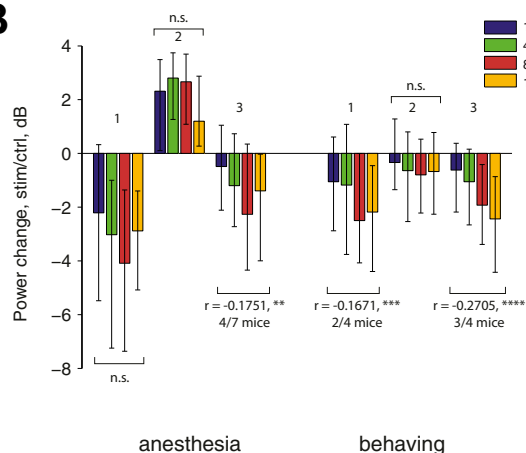
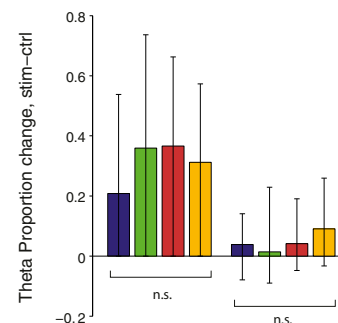
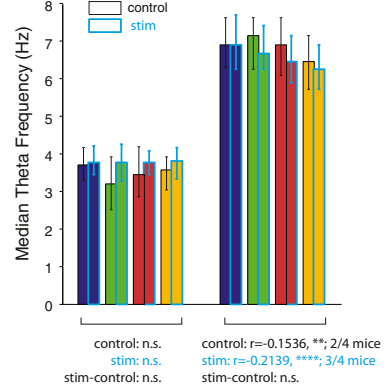
A**B****C****D**

Fig. S8. Effect of stimulation frequency. (A) LFP power changes induced by MS stimulation at 1, 4, 8, and 12 Hz (median of all trials, $n = 73, 80, 73$, and 70 , respectively, for anesthetized trials; $n = 94, 135, 96$, and 92 , respectively, for behaving trials). Numbered horizontal lines represent the subbands quantified in B. (B) Power changes in each spectrum subband: Subbands 1 (slow oscillation) and 3 (supratheta band) are significantly more affected at higher stimulation frequencies, whereas theta band (subband 2) is not. Significant correlations of stimulation frequency with the effect on each subband are indicated (Spearman's rho, $*P < 0.05$, $**P < 0.001$, $***P < 0.0001$; the number of animals in which the correlation is individually significant is indicated). (C) Theta proportion change displays a nonsignificant increase with stimulation frequency. (D) Theta frequency in theta-dominated samples in control (black outline) and stimulation (cyan outline) epochs. Significant correlations of stimulation frequency with theta frequency in control, with theta frequency during stimulation, and with the effect on theta frequency are indicated (Spearman's rho, $**P < 0.01$, $***P < 0.0001$; the number of animals in which the correlation is individually significant is indicated). We assume that higher frequency stimulation induced more spikes per unit time in the MS cholinergic neurons, and therefore enhanced the release of the amount of acetylcholine. The slight tendency that 4- and 8-Hz stimulation exerted the maximum effects in anesthetized preparation warrants further investigation, however.

Ripple trials

Theta-dominated trials

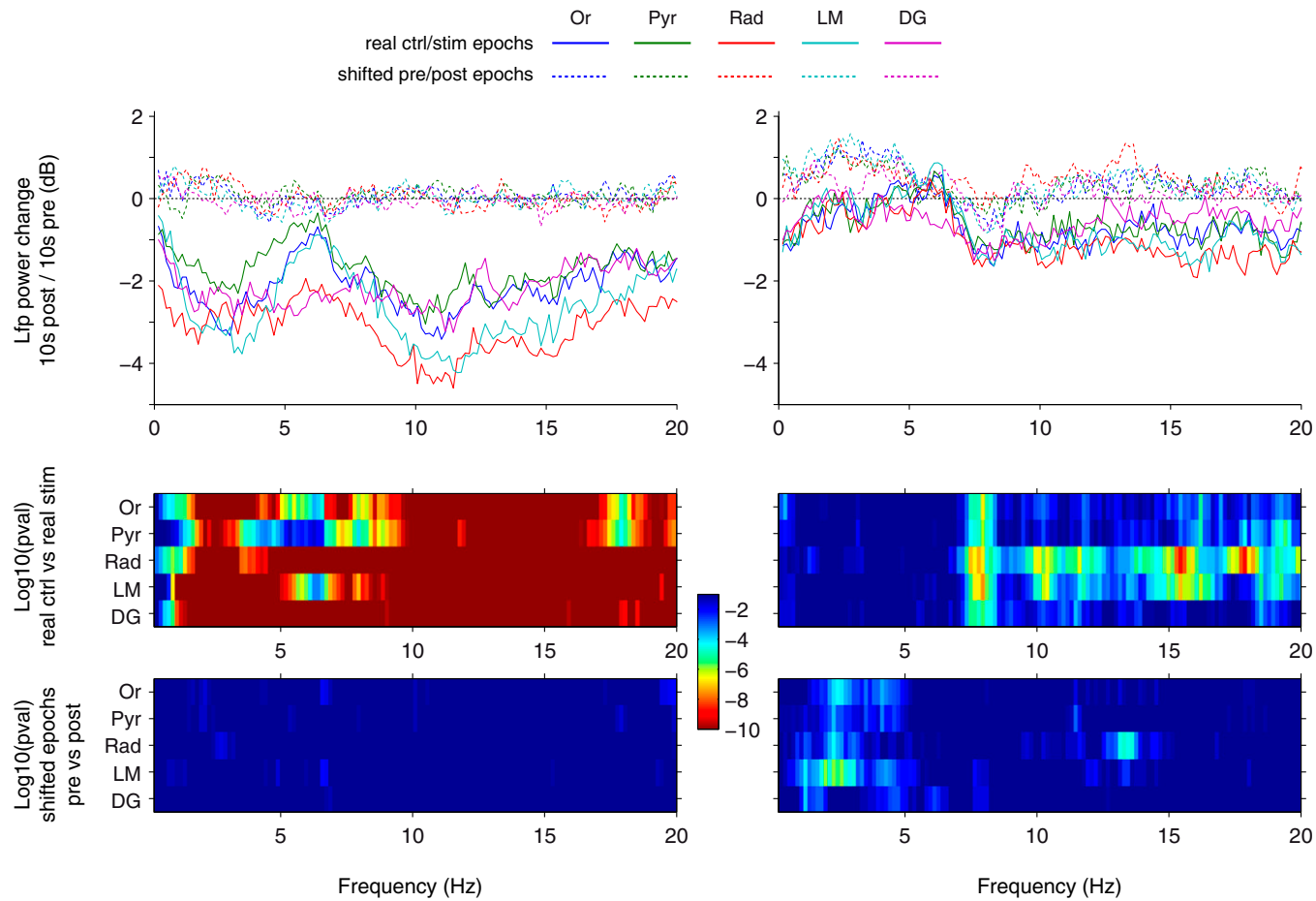


Fig. S9. Shift analysis of trial segregation effect in behaving mice. Comparison of two 10-s-long epochs starting at 10 s and 20 s before MS stimulation. (A) LFP power changes in all hippocampal layers for real control/stimulation epoch pairs (continuous lines) and shifted pre/post epoch pairs (dotted lines). (B) Color plots of significance (log of P values computed from Wilcoxon's rank sum test), computed for real control/stimulation epoch pairs (*Upper*) and for shifted pre/post epoch pairs (*Lower*) for each frequency bin in each layer.